Neoarchean environments associated with the emplacement of a large igneous province: Insights from the Carajás Basin, Amazonia Craton

Camille Rossignol, Eric Siciliano Rego, Pascal Philippot, Francesco Narduzzi, Lívia Teixeira, Marco A.L. Silva, Janaína Ávila, Cristiano Lana, Ricardo Trindade

Journal of South American Earth Sciences 130 (2023) 104574

Contents lists available at ScienceDirect

Journal of South American Earth Sciences

journal homepage: www.elsevier.com/locate/jsames

Neoarchean environments associated with the emplacement of a large igneous province: Insights from the Carajás Basin, Amazonia Craton

Camille Rossignol [a,b,*], Eric Siciliano Rego [c,d,e], Pascal Philippot [a,c], Francesco Narduzzi [a,c,f], Lívia Teixeira [a], Marco A.L. Silva [g], Janaína N. Ávila [h,i], Cristiano Lana [g], Ricardo F. Trindade [a]

[a] Departamento de Geofísica, Instituto de Astronomia, Geofísica e Ciências Atmosféricas, Universidade de São Paulo, 05508-090 São Paulo – SP, Brazil
[b] Università Degli Studi di Cagliari, Dipartimento di Scienze Chimiche e Geologiche, Cittadella Universitaria, 09042 Monserrato, Italy
[c] Géosciences Montpellier, Université de Montpellier, CNRS, Université des Antilles, Montpellier, France
[d] Instituto de Geociências, Universidade de São Paulo, 05508-080 São Paulo – SP, Brazil
[e] Origins Laboratory, Department of the Geophysical Sciences and Enrico Fermi Institute, The University of Chicago, 5734 South Ellis Avenue, Chicago, IL 60637, USA
[f] Dipartimento di Matematica e Geoscienze, Università Degli Studi di Trieste, Via Weiss 8, 34128 Trieste, Italy
[g] Applied Isotope Research Group, Departamento de Geologia, Escola de Minas, Universidade Federal de Ouro Preto, 35400-000 Ouro Preto MG, Brazil
[h] School of Earth and Environmental Sciences, The University of Queensland, St Lucia 4072, Queensland, Australia
[i] Research School of Earth Sciences, The Australian National University, 142 Mills Road, Canberra ACT 2601, Australia

ARTICLE INFO

Keywords:
Large igneous province
Banded iron formation
Paleoenvironment reconstruction
U–Pb geochronology
Chemical abrasion-LA-ICP-MS analyses

ABSTRACT

The emplacement of Large Igneous Provinces (LIPs) during the Neoarchean is thought to have influenced the Earth's surface by modulating global climate and the supply of nutrients to the oceans. However, the links between Neoarchean LIPs and Earth's surface changes are complex and not fully understood due to a lack of sedimentological constraints documenting the relationships between magmatic activity and concomitant depositional environments. At ca. 2.75 Ga, the Amazonia Craton witnessed the emplacement of the Parauapebas LIP, which is mainly composed of vesicular basalts and associated volcaniclastic rocks. The Carajás Formation conformably overlies the basalts of the Parauapebas LIP. It comprises extensive iron formations (IFs) interbedded with minor carbonate and volcaniclastic horizons, which were deposited in various shallow to deep-water settings. Zircon U–Pb dating of volcaniclastic layers yielded ages between 2732 ± 5 Ma and 2720 ± 6 Ma, which indicates that the volcanic activity continued 30–40 Myrs after the main peak in magmatic activity of the Parauapebas LIP. Above the Carajás Formation, the Igarapé Bahia Group consists mainly of terrigenous sediments that are interleaved at their base with minor IFs. This group does not preserve evidence of contemporaneous volcanic activity and comprises detrital zircon populations with ages between ca. 3.0 and 2.7 Ga. The few IFs horizons at the base of the Igarapé Bahia Group could reflect a long-lasting hydrothermal activity linked with the emplacement of the Parauapebas LIP. This LIP thus exerted a major control on depositional environments both in space and time by favoring the deposition of IFs (e.g., in shallow to deep-water settings) during a period that exceeded 30 Myrs.

1. Introduction

Emplacement of Large Igneous Provinces (LIPs) can cause large modifications to the Earth's surface environments (*e.g.*, Wignall, 2005). Neoarchean LIPs are of particular significance in that respect because they are thought to have caused irreversible changes to the Earth's atmosphere, hydrosphere and biosphere. In particular, Neoarchean LIPs fueled the deposition of massive volume of banded iron formations (BIFs) around the world by enhancing submarine hydrothermal fluxes of iron (Barley et al., 1997; Isley, 1995; Isley and Abbott, 1999; Viehmann et al., 2015). However, the causal relationship between Neoarchean LIPs and the evolution of the Earth's surface environments remains poorly understood and still a matter of debate due to a lack of detailed sedimentological work documenting the links between magmatic activity and the environmental conditions of deposition. This is in part due to a lack of preservation of sedimentary units recording the aftermaths of

* Corresponding author. Departamento de Geofísica, Instituto de Astronomia, Geofísica e Ciências Atmosféricas, Universidade de São Paulo, 05508-090 São Paulo – SP, Brazil.
E-mail address: camille.rossignol@unica.it (C. Rossignol).

https://doi.org/10.1016/j.jsames.2023.104574
Received 1 May 2023; Received in revised form 10 July 2023; Accepted 30 August 2023
Available online 7 September 2023

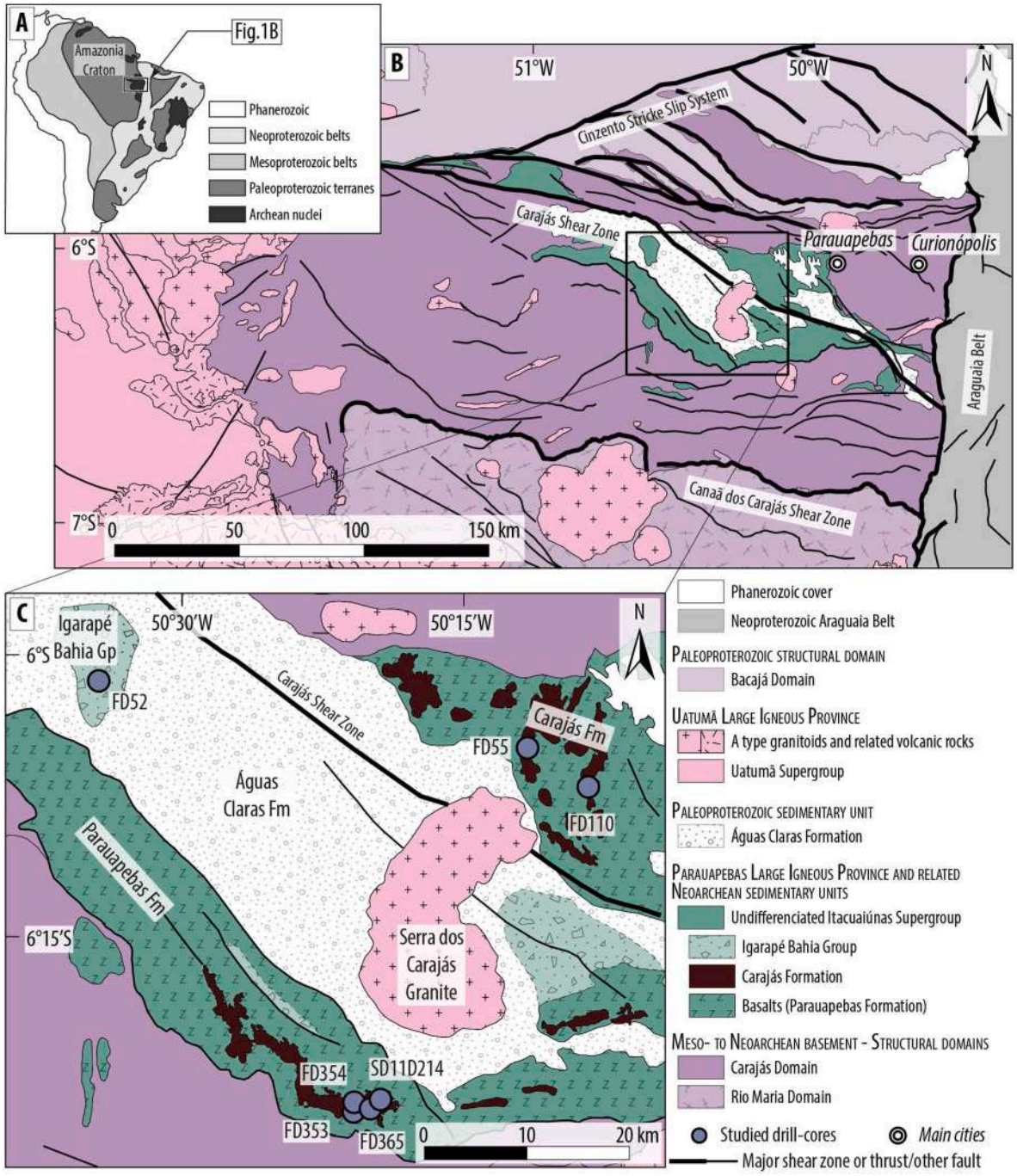

Fig. 1. Location of the Carajás Basin. **A**. Main tectonic elements of South America (Cordani et al., 2016). **B**. Geological map of the Carajás Basin (Vasquez et al., 2008). **C**. Location of the drill cores.

Neoarchean LIPs emplacement (Kump and Barley, 2007).

In the Amazonia Craton (Fig. 1A), the ca. 2.75 Ga Parauapebas LIP has recently been documented in the Carajás area (Fig. 1B and C; Rossignol et al., 2022). This area hosts some one of the largest BIF deposits worldwide (e.g., Konhauser et al., 2017). The main BIF deposits, forming the bulk of the Carajás Formation (Fig. 2) occur stratigraphically closely associated with the basalts of the Parauapebas LIP (e.g., Klein and Ladeira, 2002). However, relationships between BIF deposition and the Parauapebas LIP have not been considered. Iron deposits have also been reported in younger sedimentary units from the Carajás area, including the Igarapé Bahia Group (Fig. 2, Table 1), but the influence of the Parauapebas LIP on these BIFs remains to be evaluated. In addition, the sedimentological context for the deposition of BIFs in the Carajás area is poorly characterized and the depositional environments for these iron formations has not been studied in detail. Although the age of the Carajás IFs deposit is well defined at about 2.75 Ga (e.g., Trendall et al., 1998) as deduced from abundant age constraints on the stratigraphically associated basalts of the Parauapebas LIP, the duration of BIF deposition is unknown. The lack of constraints on the duration of BIF deposition makes any attempt to quantify the quantity of BIF that accumulated in the Carajás area contentious, and very disparate estimates have been proposed, ranging from >15 giga tons (Gt; Hagemann et al., 2016) to up to 50,000 Gt (Konhauser et al., 2017).

This study provides a detailed characterization of the topmost basalts of the Parauapebas LIP and the transition to the overlying Carajás Formation and Igarapé Bahia Group. We reconstruct of the depositional

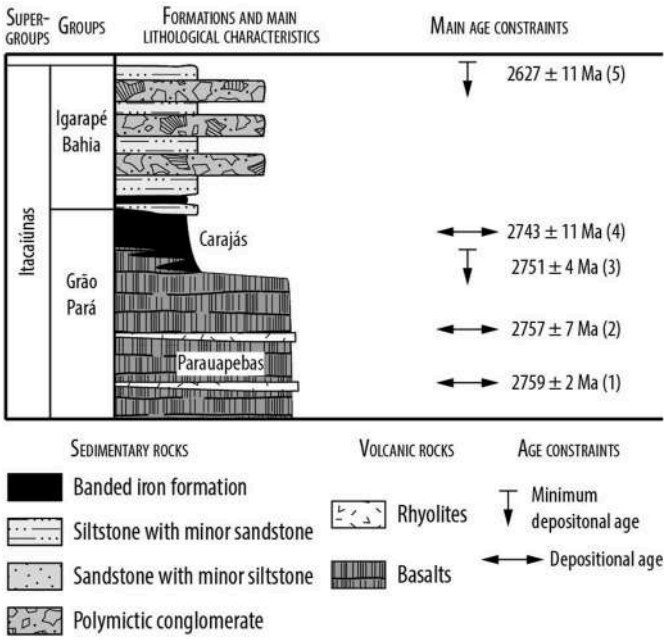

Fig. 2. Main sedimentary units of the Carajás Basin. Age constraints: Table 1.

Table 1
Summary of age constraints for the main sedimentary units of the Carajás Basin.

Number in Fig. 2	Dating method and interpretation	Reference
Parauapebas Formation		
1	U–Pb dating on zircon grains extracted from a metarhyolite: 2759 ± 2 Ma. Depositional age.	Machado et al. (1991)
2	U–Pb dating on zircon grains extracted from a metarhyolite: 2757 ± 7 Ma. Depositional age.	Trendall et al. (1998)
Carajás Formation		
3	U–Pb dating on zircon grains extracted from an intrusive sill: 2751 ± 4 Ma. Minimum depositional age.	Krymsky et al. (2007)
4	U–Pb dating on zircon grains extracted from a probable tuff: 2743 ± 11 Ma. Depositional age.	Trendall et al. (1998)
Igarapé Bahia Group		
5	Re–Os dating on molybdenite: 2627 ± 11 Ma. Minimum depositional age.	Perelló et al. (2023)
All uncertainties are given at the 2σ level.		

environments of these two sedimentary units and show that the Parauapebas LIP exerted a strong influence on nearby environments by delivering large amounts of reduced iron leading to the deposition of iron formations (IFs) in all depositional settings, from shallow to deep-water environments. New U–Pb ages obtained on thermally annealed and chemically abraded zircon grains by laser ablation - inductively coupled plasma mass spectrometry (LA-ICPMS) show that the deposition of IFs occurred over a period of at least 30–40 Myrs, which further support the long-lasting impact of the LIP emplacement on nearby sedimentary systems.

2. Geological setting

2.1. Regional context

The Carajás Basin is located in the Carajás Domain (Fig. 1B), which is made up of polymetamorphic tonalitic to granodioritic gneisses and migmatites with protolith ages of ca. 3080 Ma to ca. 3000 Ma (Machado et al., 1991; Moreto et al., 2015b; Pidgeon et al., 2000). The basement was later intruded by tonalites, trondhjemites, and granodiorites (TTG) between ca. 2960 Ma and ca. 2930 Ma (Feio et al., 2013), between ca. 2870 Ma to 2830 Ma (Feio et al., 2013; Machado et al., 1991; Moreto et al., 2015b; Pidgeon et al., 2000), and at 2820 ± 22 Ma (Feio et al., 2013). A long-lasting tectono-thermal event identified by granitoid emplacement and coeval hydrothermal activity occurred between ca. 2600 and 2450 Ma (Machado et al., 1991; Melo et al., 2017; Requia et al., 2003; Tallarico et al., 2005; Toledo et al., 2019).

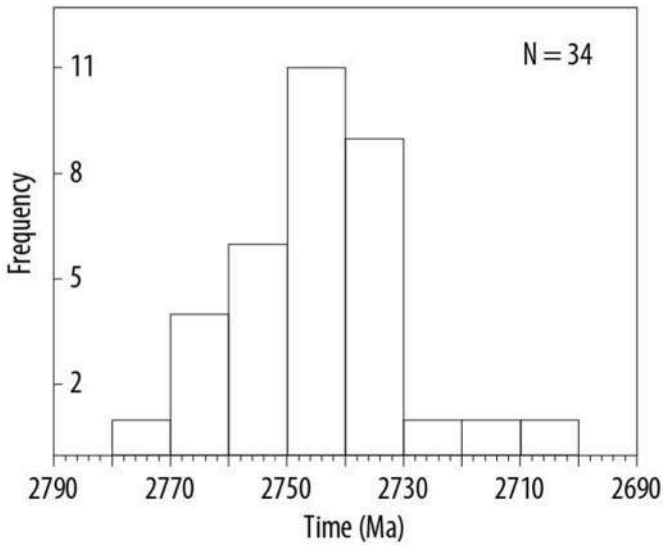

Fig. 3. Frequency distribution of zircon U–Pb dates of rocks from the Parauapebas Large Igneous Province. Data source: Table 2. Bin width: 10 Ma.

To the north, the Bacajá Domain is mainly made up of Rhyacian granitoids intruded in a tonalitic basement with a protolith age of ca. 2670 Ma (Macambira et al., 2009). To the south the Rio Maria Domain comprises Mesoarchean greenstone belts with komatiites (Siepierski and Ferreira Filho, 2016) and TTG emplaced between ca. 2980 and ca. 2920 Ma (Almeida et al., 2013) and between ca. 2870 Ma and ca. 2860 Ma (Almeida et al., 2013; Feio et al., 2013). The Rio Maria and the Carajás Domain were accreted since the end of the Mesoarchean, between ca. 2.87 Ga and ca. 2.83 Ga. To the west, the Carajás Basin is overlain by volcanic and volcaniclastic rocks of the Uatumã Supergroup of the ca. 1.88 Ga Uatumã Silicic LIP (Antonio et al., 2017, 2021) while the eastern boundary of the basin is obliterated by the Neoproterozoic Araguaia Belt (Fig. 1B).

At the end of the Neoarchean and during the Paleoproterozoic, different tectonic events affected the basement and overlying sediments, forming a WNW oriented strike-slip system (Pinheiro and Holdsworth, 1997; Tavares et al., 2018; Toledo et al., 2019). Major shear zones are sealed by the ca. 1.88 Ga granitoids (Fig. 1C), and the Carajás Basin was subjected to minor tectonic and magmatic events afterward (e.g., Tavares et al., 2018).

2.2. Parauapebas LIP

Around ca. 2.75 Ga, important mafic magmatism produced a 4–6 km thick basaltic series forming the Parauapebas Formation (Fig. 3; Table 2; Lacasse et al., 2020; Machado et al., 1991; Martins et al., 2017; Olszewski et al., 1989; Toledo et al., 2019; Trendall et al., 1998; Wirth et al., 1986). Because the Parauapebas Formation has been largely eroded, it is difficult to assess the exact areal extent, but present-day outcrops and inliers suggest that it covered a large part of the southeast Amazonia Craton (Souza et al., 2020; Vasquez et al., 2008). Associated with the basalts are layered ultramafic and mafic plutons, as well as A-type granitoids (Feio et al., 2013; Machado et al., 1991; Mansur and Ferreira

Table 2
Summary of reported ages from ultramafic, mafic and alkaline intraplate felsic rocks from the Parauapebas Large Igneous Province.

Rock type	Rock unit	Material	Method	Age (Ma)	Uncertainties (2σ level)	Reference
Plutonic rocks						
Anorthositic gabbro	Luanga	Zircon	U–Pb	2763	6	Machado et al. (1991)
Syenogranite	Planalto	Zircon	U–Pb	2729	17	Feio et al. (2012)
Syenogranite	Planalto	Zircon	U–Pb	2710	10	Feio et al. (2012)
Syenogranite	Planalto	Zircon	U–Pb	2706	5	Feio et al. (2012)
Gabbro	Planalto	Zircon	U–Pb	2735	5	Feio et al. (2012)
Gabbronorite		Zircon	U–Pb	2739	6	Moreto et al. (2015b)
Granite	Sossego	Zircon	U–Pb	2740	26	Moreto et al. (2015b)
Granite	Cural	Zircon	U–Pb	2739	4	Moreto et al. (2015b)
Syenogranite	Planalto	Zircon	U–Pb	2738	3	Feio et al. (2013)
Syenogranite	Planalto	Zircon	U–Pb	2730	5	Feio et al. (2013)
Trondjhemite	Pedra Branca	Zircon	U–Pb	2750	5	Feio et al. (2013)
Granodiorite to syenogranite	Igarapé Gelado	Zircon	U–Pb	2763	4	Melo et al. (2017)
Granitoid		Zircon	U–Pb	2741	5	Moreto et al. (2015a)
Granitoid		Zircon	U–Pb	2745	4	Moreto et al. (2015b)
Granite	Bom Jesus	Zircon	U–Pb	2739	9	Borba et al. (2021)
A-type granite	Planalto	Zircon	U–Pb	2739	19	Borba et al. (2021)
A-type granite	Serra do Rabo	Zircon	U–Pb	2743	2	Sardinha et al. (2006)
Enderbite	Café	Zircon	U–Pb	2730	7	Marangoanha et al. (2019a)
Enderbite	Café	Zircon	U–Pb	2740	8	Marangoanha et al. (2019a)
Monzogranite	Vila União	Zircon	U–Pb	2744	22	Marangoanha et al. (2019b)
Diorite	Vila União	Zircon	U–Pb	2735	18	Marangoanha et al. (2019b)
Monzogranite	Vila União	Zircon	U–Pb	2745.3	14.2	Marangoanha et al. (2020)
Tonalite	Vila União	Zircon	U–Pb	2745.8	19.8	Marangoanha et al. (2020)
Volcanic rocks						
Rhyodacite	Parauapebas Formation	Zircon	U–Pb	2759	2	Machado et al. (1991)
Rhyolite	Parauapebas Formation	Zircon	U–Pb	2759	2	Machado et al. (1991)
Rhyolite	Parauapebas Formation	Zircon	U–Pb	2760	11	Trendall et al. (1998)
Rhyolite	Parauapebas Formation	Zircon	U–Pb	2757	7	Trendall et al. (1998)
Basalt	Parauapebas Formation	Zircon	U–Pb	2751.4	3.7	Krymsky et al. (2007)
Basalt	Parauapebas Formation	Zircon	U–Pb	2749.6	6.5	Martins et al. (2017)
Basalt	Parauapebas Formation	Zircon	U–Pb	2745	5	Martins et al. (2017)
Rhyolite	Parauapebas Formation	Zircon	U–Pb	2758	39	Wirth et al. (1986)
Volcanic rocks	Parauapebas Formation	Zircon	U–Pb	2748	34	Tallarico et al. (2005)
Metamorphosed mafic rocks (protolith age)						
Amphibolite	Salobo Group	Zircon	U–Pb	2761	3	Machado et al. (1991)
Amphibolite		Zircon	U–Pb	2774	19	Toledo et al. (2019)

Filho, 2016; Marangoanha et al., 2019a, 2019b, 2020; Sardinha et al., 2006; Siepierski and Ferreira Filho, 2020). These magmatic rocks were emplaced in an intraplate tectonic setting (Olszewski et al., 1989; Feio et al., 2012; Martins et al., 2017; Toledo et al., 2019; Lacasse et al., 2020). The bulk of the Parauapebas volcanism occurred around 2.75 Ga (Gibbs et al., 1986; Machado et al., 1991; Martins et al., 2017; Olszewski et al., 1989; Toledo et al., 2019; Trendall et al., 1998). All these characteristics portray the Parauapebas volcanics and associated intrusive rocks as a typical LIP (Rossignol et al., 2022).

2.3. Stratigraphic framework

The sedimentary units overlying the Parauapebas LIP consist of the Carajás Formation and the Igarapé Bahia Group (Fig. 2). The Carajás Formation is mainly made up of BIFs (Dalstra and Guedes, 2004; Klein and Ladeira, 2002; Tolbert et al., 1971) and minor black shales and conglomerates (Cabral et al., 2017). Microstructures of probable biogenic origin have been identified (Ribeiro da Luz and Crowley, 2012), concurring with Fe and C isotope data suggesting that the deposition of the IFs was mediated by anoxygenic photosynthetic organisms (Rego et al., 2021). The absence of cerium anomalies indicates anoxic conditions during IF deposition, while extreme europium anomalies imply input of high-temperature hydrothermal fluids into seawater (Rego et al., 2021). The very low content of lithophile elements in IFs suggests that the Carajás Formation was deposited far away from emerged lands (Justo et al., 2020; Macambira and Schrank, 2002; Martins et al., 2021). The interlayering of volcanic rocks and BIFs shows that the Carajás Formation was deposited, at least in part, coevally with the Parauapebas LIP (Gibbs et al., 1986; Martins et al., 2017). The Carajás Formation is younger than 2759 ± 2 Ma, corresponding to the emplacement age of underlying volcanic rocks (Table 1; Machado et al., 1991). Dolerite sills intruded some BIFs at 2751 ± 4 Ma (Krymsky et al., 2007) and 2740 ± 8 Ma (Table 1; Trendall et al., 1998).

The Carajás Formation is overlain by the Igarapé Bahia Group (Fig. 2). The contact between these two units has not been observed but is generally assumed to be concordant (Araújo et al., 2021). However, the Igarapé Bahia Group directly overlies the basalts of the Parauapebas Formation in some localities, suggesting that the Igarapé Bahia Group could overlie discordantly the Carajás Formation (Dreher et al., 2005; Melo et al., 2019). At its base, the Igarapé Bahia Group comprises BIF layers up to 10 m thick, grading upward to sandstone and siltstone interbedded with polymictic conglomerate containing angular clasts of BIF, chert, and volcanic rocks (Dreher et al., 2005, 2008; Galarza et al., 2008; Melo et al., 2019; Ronze et al., 2000). Re–Os dating on molybdenite indicates that the Igarapé Bahia Group has been deposited before 2627 ± 11 Ma (Table 1; Perelló et al., 2023).

3. Methodology

3.1. Sedimentological analyses and sampling

Seven fully cored wells were studied (Fig. 1C, Appendix 1), among which six intercept the Carajás Formation (FD55, FD110, FD353, FD354, FD365 and S11D214) and one (FD52) intersects the Igarapé Bahia Group. Three wells (FD55, FD110 and FD353) also intercept the topmost part of the Parauapebas Formation and are used to provide a description of the basalts and their contact with the overlying Carajás Formation. The drill cores were surveyed and logged at the 1/500 to 1/

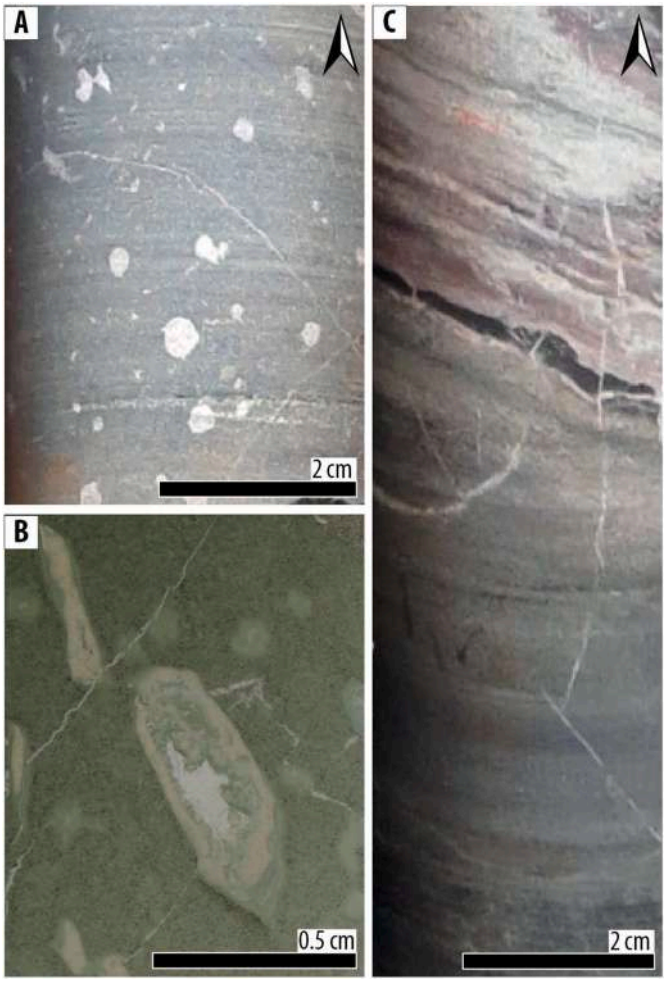

Fig. 4. Basalts and volcaniclastic rocks of the Parauapebas Formation. Arrows point to the stratigraphic top. **A.** Sample FD55 535.45. Basaltic layer with large vesicles. **B.** Sample FD55 527.72. Slide scan image of a thin section showing amygdaloidal basalt with elongated vesicles filled up with chlorite and calcite. **C.** Contact between the spilitized basalts of the Parauapebas Formation and BIFs of the Carajás Formation.

100 scales to identify their sedimentary facies. Lithology, sedimentary structures, petrography, clast lithology and shape, grading, syn-sedimentary deformational structures, and nature of the bedding contacts between successive facies are described below.

The mineralogy was determined petrographically by reflected and transmitted light microscopy, complemented by scanning electron microscopy (SEM) and energy dispersive X-ray spectroscopy (EDS) for semi-quantitative SEM-EDS analysis. Three volcaniclastic samples from the Carajás Formation and four sandstone and conglomerate samples from the Igarapé Bahia Group were collected for zircon U–Pb dating. Different sedimentary facies were sampled in order to minimize potential bias associated with sediment transport (Lawrence et al., 2011).

3.2. U–Pb zircon geochronology

3.2.1. Analytical methods

The zircon grains were extracted following a classical mineral separation procedure and handpicked under a binocular microscope. Zircon crystals from the Carajás Formation were subjected to a thermal annealing and chemical abrasion (TACA) treatment before Laser Ablation – Inductively Coupled Plasma – Mass Spectrometry (LA-ICP-MS) analysis following the procedure detailed in Rossignol et al. (2022). After embedding the grains in epoxy resin, the pucks were hand grounded to reveal equatorial cross-sections and imaged by cathodoluminescence to choose laser microsampling sites. No TACA treatment has been applied to zircon grains from the Igarapé Bahia Group, because of the limited number of zircon grains extracted in these samples (N = 28 to 38; Appendix 2). A detailed analytical set-up is given in Appendix 2. Potential biases related to the TACA treatment have been controlled by comparing untreated and TACA grains from the same samples and appears limited in this study (Appendix 2).

3.2.2. Age calculations and data filtering

Data were filtered using their probability of concordance (Ludwig, 1998) with a cut-off level of 10% including decay constant errors (Rossignol et al., 2016). Concordant analyses (probability of concordance $\geq$10%) were kept for calculating maximum depositional ages (MDAs) as the concordia age of the youngest cluster of at least 3 grains using Isoplot 3.00 (Ludwig, 1998, 2012). Uncertainties are quoted at the 95% confidence level.

4. Sedimentary facies analyses

4.1. Basalts and associated volcaniclastic rocks of the Parauapebas Formation

The basalts of the Parauapebas Formation comprise mm-to cm-size amygdales commonly filled with quartz, calcite and chlorite (Fig. 4A and B). The contact between the Parauapebas Formation and the overlying Carajás Formation is sharp and conformable (Fig. 4C).

4.2. Carajás Formation

Ten facies were recognized (Fig. 5; Table 3), defining three facies associations (Table 4). Representative BIF facies are presented in Fig. 6. Diagenetic and syn-depositional deformations are shown in Fig. 7, granular iron formations and conglomerates in Fig. 8, and carbonate facies in Fig. 9.

4.2.1. Facies association 1

4.2.1.1. Description. The most common facies consists of BIFs (I1; Table 3) made up of alternating layers of Fe-rich minerals (magnetite and hematite) and chert with microcrystalline quartz and a few ankerite minerals disseminated in the matrix. Laminations are mm-to cm-thick and usually exhibit an even banding (Fig. 6A). Some laminations, however, display wavy structures (Fig. 6B), pinching geometries and erosion surfaces (Fig. 6C). The bedding is horizontal, but some layers show abrupt changes in bed orientation, suggesting slumped structures. Diagenetic features in the I1 facies comprise inflated beds that form cm-thick magnetite layers parallel to the bedding (Fig. 7A) and a few layers comprise secondary minerals (Fig. 7B). Association 1 comprises two other less common IF facies (I2 and I3; Table 3). I2 facies has a similar lithology to I1 facies but exhibits chaotic structures (Fig. 7C). Granular Iron Formation (GIF; I3 facies) consists of cm to tens of cm-thick beds comprising very elongated clasts (1:5 width to length ratio, with largest clasts of cm scale), generally with rounded to sub-rounded ends (Fig. 8A). GIF beds are ungraded to normally graded and are interbedded within the I1 facies (Fig. 8B). The clasts locally display buckled shapes attesting plastic deformation during transport and are generally flattened parallel to bedding (Fig. 8A, C). Association 1 also comprises matrix-supported ironstone flat-pebble conglomerate (G1; Table 3). The pebbles are elongate (up to 10 cm long) intraformational rip-up clasts with sub-angular and cuspate shapes (Fig. 8D). Some clasts have sub-rounded to rounded ends (Fig. 8B and C), showing that they experienced various degrees of reworking. The clasts are generally flattened parallel to bedding (Fig. 8D and E). As being intraformational, most of the clasts are made up of chert or silicate-rich BIF, while a few are made

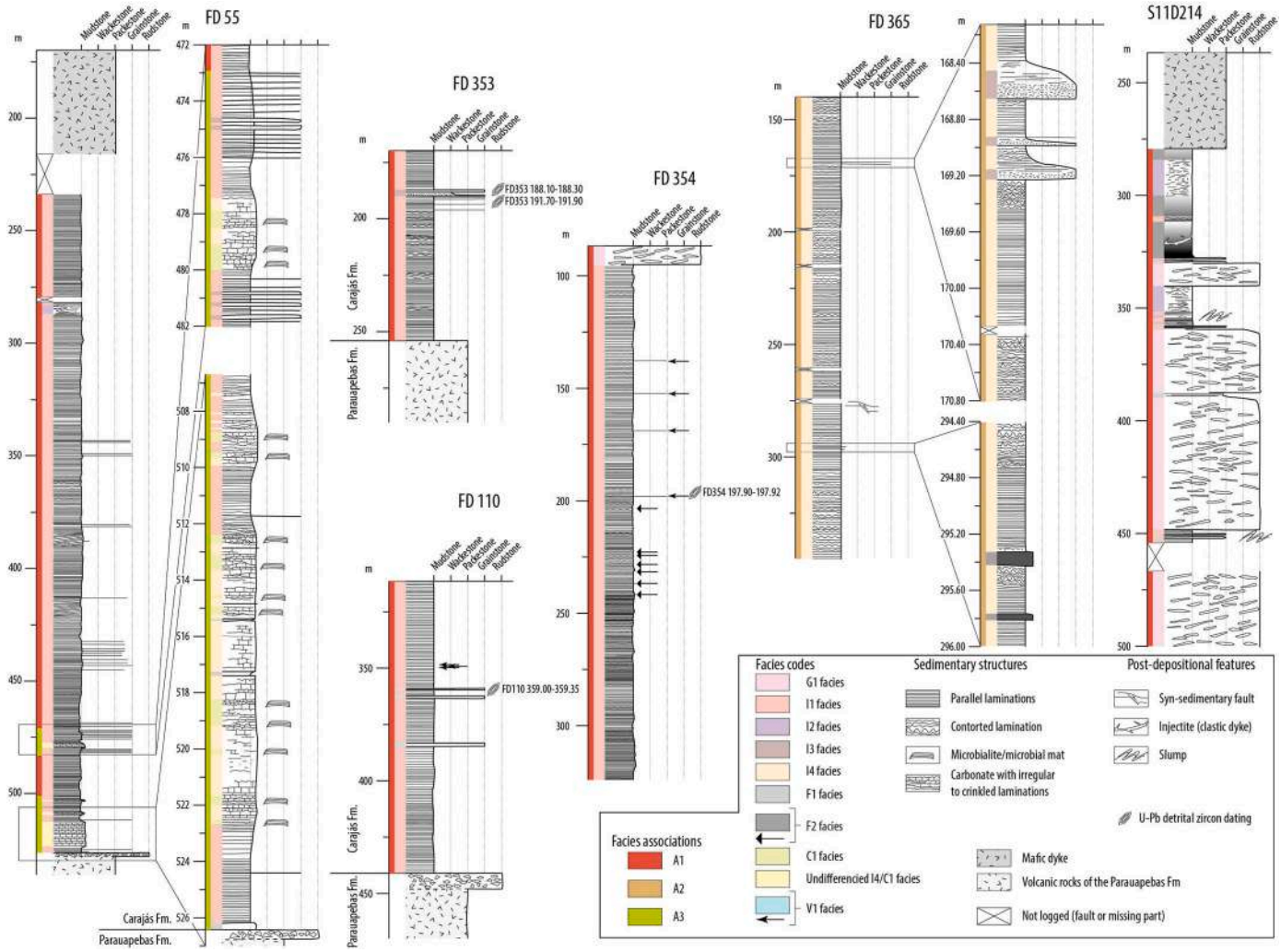

Fig. 5. Sedimentological logs of the drill cores intersecting the Carajás Formation. Facies codes: Table 3. Facies associations: Table 4.

up of GIF (Fig. 8F and G) or greenish sandstones. The conglomerate beds are up to tens of meters thick, ungraded to normally graded, and have non-erosive bases. Minor facies in association 1 are represented by a few black shale beds (F2; Table 3) that are commonly deformed and intruded by clastic dykes (Figs. 7F), 1-5 cm-thick greyish claystone layers, and a few m-thick beds made up of greenish, chlorite-rich, strongly weathered basaltic sandstone (V2; Table 3). These layers, without apparent sedimentary structure, are interbedded, in sharp contact with BIFs, and contain zircon grains.

4.2.1.2. Interpretation. The prevalence of finely laminated BIF suggests a deposition by settling of Fe-rich chemical mud in a deep-water environment, below storm wave-base (Table 4; Klein, 2005; Trendall, 2002). The sedimentary structures in BIFs, such as erosion surfaces, also attest for current reworking of fine-grained sedimentary particles and suggest deposition by turbidity currents (Dimroth, 1975; Rasmussen et al., 2013). Inflated beds formed during late diagenesis by seepage of reducing fluids that remobilized Fe along fractures oriented parallel to the bedding (Czaja et al., 2018). The few GIF layers interbedded within BIFs are also indicative of turbidity currents reworking chert clasts coarser than the silt-sized elements forming the main BIF deposits (Rasmussen et al., 2013; Simonson and Goode, 1989). The occurrence of chaotic beds is interpreted as slumps (Martinsen, 1994) and compares with previous observations of slumps in similar facies of the same formation (Martins et al., 2021). G1 facies is interpreted to be deposited by the failure, induced either by storm or seismic activity, of loosely consolidated deposits (Myrow et al., 2004). Clastic dykes indicate rapid deposition from short-lived flows (*i.e.*, subaqueous mass flow during the deposition of conglomerates) or liquefaction related to seismicity. The occurrence of black shale suggests that biological activity was high. Volcanic and volcaniclastic beds indicate episodic volcanic inputs. Several cm-thick greyish clay beds are interpreted as diagenetic ashes formed as fallout deposits emitted by distal volcanic centers (Sohn et al., 2008). Thicker beds of basaltic sandstone can correspond either to hyaloclastic deposits with limited transport of the volcaniclasts, or to subaqueous debris flow reworking basaltic volcaniclasts (Sohn et al., 2008).

4.2.2. Facies association 2

4.2.2.1. Description. This association comprises mainly carbonate-rich BIFs (I4, Table 3) exhibiting sedimentary structures that are essentially like those of the I1 facies, with horizontal to wavy laminations and reactivation surfaces (Fig. 6D). Carbonate-rich BIFs are made up of magnetite interlayered with ankerite and chert layers and containing a few Fe-silicate and pyrites. Minor facies of association 2 consist of GIF (I3) and black shales (F2). Carbonate-rich BIFs exhibit numerous syn-sedimentary ductile deformation features marked by contorted laminations (Fig. 7D) and syn-sedimentary faults occurring together with angular intraformational clasts (Fig. 7E).

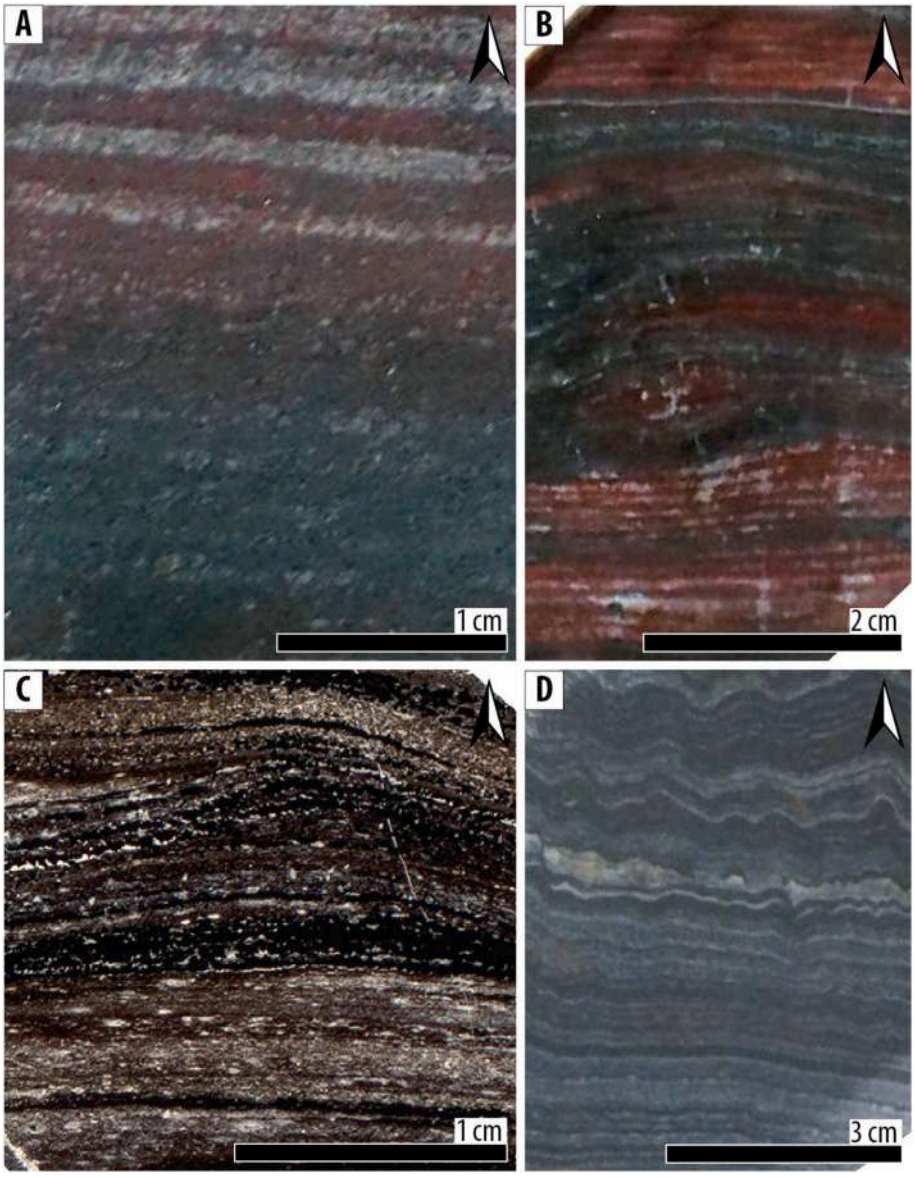

Fig. 6. Banded iron facies from the Carajás Formation. Arrows point to the stratigraphic top. **A.** Sample FD55 486.45. Fine horizontal laminations (sub-mm scale) of Fe-bearing minerals (magnetite and hematite) and chert layers. **B.** Sample FD55 495.80. Finely laminated siliceous BIF displaying wavy laminations. **C.** Sample FD55 480.80. Thin section in reflected light showing a reactivation surface in a jaspilitic BIF. **D.** Sample FD365 182.70. Alternating layers of Fe-rich minerals and carbonates (carbonate-rich BIF; facies I4) with wavy irregular laminations.

4.2.2.2. Interpretation. The overall characteristics of association 2 are similar to those of association 1, suggesting a rather similar deep-water environment, below wave base (Table 4). The precipitation of carbonate can be explained by deposition above the carbonate compensation depth, climate change to warmer temperatures (Beukes, 1983), change to more alkaline pH sea-water (Spier et al., 2007), or change in organic carbon input, allowing organic carbon to be exported from highly productive surface water and mineralized in deeper parts of the basin (Craddock and Dauphas, 2011; Heimann et al., 2010; Johnson et al., 2013). Because the studied drill cores do not show the relationship between facies association 2 and other facies associations, it is difficult to infer which of the above-mentioned processes favored the precipitation of carbonate. Based on other basins comprising similar facies, the likely depositional environment for association 2 is similar to that of association 1, but in a more proximal (shoreward) and shallower setting (Beukes and Gutzmer, 2008; Smith et al., 2013). The occurrence of numerous syn-sedimentary ductile and brittle deformation features indicates slope instability leading to the formation of slumps or slides (Martinsen, 1994).

4.2.3. Facies association 3

4.2.3.1. Description. This facies association comprises carbonate-rich BIF (I4) with even banded (Fig. 9A), wavy (Fig. 9B) and irregular layers (Fig. 9C), grading to facies C1 (Table 3), which is mainly made up of mm-to cm-thick wavy to crinkly carbonates laminae and minor iron oxides (Fig. 9D and E). Carbonates in facies C consist of ankerite and calcite, but also contain framboidal pyrite, magnetite, chert, Fe-silicate and organic matter (Fig. 9F and G). The I4 and C1 beds alternate with silica-rich BIF (I1). Association 3 also comprises numerous GIF beds up to ten cm-thick, occurring a few meters below and above I4 and C1 beds. A few cm-thick beds made up of dark and fine-grained sediments also occur (F1; Table 3).

4.2.3.2. Interpretation. The occurrence of crinkly laminae, framboidal pyrites and organic matter in facies C1 are indicative of microbially induced sedimentary structures (MISS), suggesting a shallow-water setting typical of the photic zone, above wave base (Table 4; Hagadorn and Bottjer, 1997; Noffke et al., 2001). This is consistent with the contribution of microbial anoxygenic photosynthesis to the precipitation of iron formations and carbonates in the Carajás Formation (Rego

Table 3
Sedimentary facies of the Carajás Formation and Igarapé Bahia Group.

Code	Lithology	Sedimentary structures	Depositional processes
Iron-rich facies			
I1	Alternating layers of Fe-rich minerals and chert (microcrystalline quartz) or jasper (i.e., chert with minor, disseminated microcrystalline hematite; Fig. 6A, B, C). Thickness of chert BIF intervals: m to hundreds of m.	Banding over a range of scale, from meters (macrobands), centimeters (mesobands) to millimeters and sub-millimeters layers (microbands). The laminations are generally evenly layered (Fig. 6A), but sometimes display a wavy (Fig. 6B), irregular banding, or exhibit reactivation surfaces (Fig. 6C). The layers sometimes display diagenetic inflated beds (Fig. 7A) and secondary mineralization (Fig. 7B).	Deposition from suspension of a Fe-rich chemical mud (Dimroth, 1975; Klein, 2005; Trendall, 2002) or by turbidity current (Dimroth, 1975; Rasmussen et al., 2013).
I2	Chert, siliceous BIF or carbonate BIF. Bed thickness: m to tens of m.	Chaotic horizons, disordered or strongly folded (Fig. 7C). Intraformational angular clasts occur at slip surfaces. Syn-sedimentary faults (Fig. 7E).	Slump and/or slide (Martinsen, 1994).
I3	Granular Iron Formation comprising very elongated (Fig. 8A) to rather spherical grains (Fig. 8B and C), mainly sub-angular to sub-rounded, made up of cherty material very similar to the one of the I1 facies. Bed thickness: cm to dm.	Ungraded or normally graded. When elongated micro-clasts are present, they show an orientation and are flattened parallel to the bedding (Fig. 8C). Some clasts are bended or ductilely deformed.	Rip-up clasts redeposited by turbidity current and/or bottom return flow induced by storms (Simonson and Goode, 1989).
I4	Alternating layers of Fe-rich minerals (mainly magnetite) and carbonate (Fig. 6D) with minor amount of chert. Thickness of carbonate BIF intervals: cm to hundreds of m.	Banding over a range of scale (macrobands, mesobands and microbands). The laminations range from a finely and regularly laminated structure to weak and irregular magnetite layers. The layers commonly display syn-sedimentary micro-folding (Fig. 6D) or reactivation surfaces (Fig. 7E).	Similar to I1 facies above the carbonate compensation depth, under warmer climate, which favor carbonate over chert precipitation (Beukes, 1983), or in more alkaline water (Spier et al., 2007), or under a high organic carbon input which contributed as the source of carbon for carbonate precipitation (Craddock and Dauphas, 2011).
Conglomerate			
G1	Matrix-supported ironstone flat pebbles conglomerate. Clasts are mainly elongated and angular (Fig. 8D) but some have sub-rounded to rounded ends (Fig. 8E). Clasts are mainly made up of BIF or chert. A few clasts are made up of GIF (Fig. 8F and G) or greenish sandstone. Ferruginous, greenish to reddish matrix. Bed thickness: m to tens of m.	Ungraded to normally graded. The clasts exhibit an orientation (Fig. 8D and E). Some clasts are slightly curved to strongly bended (Fig. 8D, E, G). Non-erosive base.	Failure and mass movement of loosely consolidated sediments (Myrow et al., 2004).
G2	Flat-pebbles conglomerate, matrix- to clast-supported. Clasts are elongated and generally exhibit sub-rounded to rounded shapes, with a few sub-angular clasts (Fig. 11A, B, C). Clasts are intraformational and made up of sand, silt to clay, or a mixture of sand and silts (Fig. 11D). The matrix is made up of similar material. Bed thickness: tens of cm to m.	Generally ungraded but sometimes with inverse, normal or inverse to normal grading. The clasts generally exhibit an orientation and are flattened parallel to the bedding (Fig. 11A, E). Generally non-erosive base (Fig. 11E). A few beds have a slightly erosive base.	Failure and mass movement of loosely consolidated sediments and/or wave or storm reworking of shoreline deposits (Myrow et al., 2004).
Sandstone and Fine			
S1	Fine to very coarse sand (Fig. 12A) with floating clasts (granules to pebbles, sometimes intraformational muddy ripped up clasts; Fig. 12B). Occurrence of contorted sandy to muddy rafts (Fig. 12D). Bed thickness: dm to m.	Massive or normal grading, sometimes with horizontal planar bedding. Few occurrences of contorted beds.	Hyper-concentrated density flow to turbidity flow (Mulder and Alexander, 2001) or rapid suspension fallout (Postma, 1990).
S2	Various lithologies, mainly sand and silt. Thickness: tens of cm to m.	Chaotic horizons, sometimes forming anastomosed elutriation bands (Fig. 12E), or strongly folded beds (Fig. 12F).	Slump and/or slide (Martinsen, 1994), deformation induced by water escape (Ravier et al., 2015).
F1	Greyish to greenish siltstone, fine to medium sandstone Bed thickness: cm to tens of cm.	Generally horizontal laminations, sometimes massive.	Deposition from suspension.
F2	Darkish siltstone to claystone. fine to medium sandstone Bed thickness: cm to tens of cm.	Apparently massive. Sometimes crosscut by injectites (clastic dyke; Fig. 7F)	Deposition from suspension.
Volcaniclastic			
V1	Greyish clay layers, sometimes containing a few zircon grains, and greenish sandstone layers. Bed thickness: cm (clays) to m (greenish sandstone).	No apparent sedimentary structure. Sharp contacts with under- and overlying BIF.	Diagenetic volcanic ashes, potentially reworked, or subaqueous debris flow reworking volcaniclasts (Sohn et al., 2008).
Carbonates			
C1	Carbonate (ankerite, calcite; Fig. 9G) comprising a few pyrite (Fig. 9F), iron oxides (mainly magnetite; Fig. 9G), and micritic texture (Fig. 9E). Continuous transition between C and I4. Thickness: dm to m.	mm to cm-thick parallel (Fig. 9A), crinkled, wavy (Fig. 9D), or irregular layering (Fig. 9C). Laminations are underlined by oxide layers ranging from cm-thick to very tiny (mm-thick) and discontinuous magnetite layers. Magnetite beds sometimes exhibit pinching geometries or underline wavy laminations (Fig. 9B).	Microbial mats or stromatolites (Hagadorn and Bottjer, 1997; Noffke et al., 2001) alternating with background carbonate sedimentation.
C2	Alternation of carbonate-rich layers with fine terrigenous sand beds or fine magnetite layers. Thickness: dm to m.	Thinly laminated, with evidence of post-depositional deformations (Fig. 12G and H).	Sediments deposited during periods of low detrital input, allowing for the deposition of carbonate and iron-rich layers.

et al., 2021). The numerous GIF beds below and above MISS alternating with I1 and minor F1 facies indicate an intermittent energetic environment allowing for reworking clasts ripped up from loosely lithified cherts (Simonson and Goode, 1989).

4.3. Igarapé Bahia Group

The Igarapé Bahia Group is intersected by the drill core FD52 (Fig. 10). Six sedimentary facies were identified (Table 3) and grouped in two facies associations (Table 4).

Table 4
Facies associations of the Carajás Formation and Igarapé Bahia Group.

Code	Facies association	Depositional environment
Carajás Formation		
A1	I1 with minor occurrences of G1, I1 and I2, I3, F2 and rare occurrences of I4, and V2.	Probably below storm wave-base (Klein, 2005; Rasmussen et al., 2013; Trendall, 2002). Episodic volcanic inputs and reworking of volcanic loosely lithified volcanic deposits by subaqueous debris flow suggest a coeval volcanic activity (Sohn et al., 2008).
A2	I4 with rare occurrences of I3 and F2.	Similar to A1, but in a more proximal (shoreward) and shallower setting (Beukes and Gutzmer, 2008; Smith et al., 2013).
A3	I4 and C1 with occurrences of I1, I3 and rare occurrence of F1.	Shallow-water environment (photic zone) shown by the presence of photosynthetic organisms in C1 facies (Rego et al., 2021) and microbially-induced sedimentary structures (Hagadorn and Bottjer, 1997; Noffke et al., 2001). Intermittent reworking of poorly lithified material suggesting a rather high-energy environment (Simonson and Goode, 1989).
Igarapé Bahia Group		
A4	G2, S1, S2, F1 and F2.	Offshore environment (Myrow et al., 2004), important terrigenous influx.
A5	C2, S1 and F1.	Similar to A4, but with lower terrigenous input allowing for the development of iron-rich facies.

4.3.1. Facies association 4

4.3.1.1. Description. The main facies consists of clast-to matrix-supported flat-pebble conglomerate made up of tens of cm to m-thick beds (facies G2; Table 3). The matrix comprises fine sand, silt or clay. The clasts are intraformational (Fig. 11A, B, C) and some preserves laminated structures (Fig. 11D). Most of the clasts are elongate (a few cm to tens of cm long), flattened parallel to the bedding (Fig. 11E) and with rounded ends, although a few clasts are sub-angular. Conglomeratic beds have a non-erosive base (Fig. 11E) and are generally ungraded, although some of them display a normal, inverse or inverse to normal grading. Facies G2 is interbedded with finer lithologies composed of sand (S1 and S2; Table 3) and silt to clay (F1 and F2; Table 3). Sand facies are coarse-to fine-grained (Fig. 12A, B, C), commonly comprise intraformational muddy rip up clasts (Fig. 12B), contorted sandy to muddy rafts (Fig. 12D), and consists of tens of cm to m-thick beds. Beds of S1 facies are either ungraded or normally graded and sometimes exhibit horizontal laminations. Horizons of S2 facies are characterized by chaotic stratification. Some horizons display anastomosed elutriation bands resulting from escaping water and elutriation of fine particles along vertical conduits (Fig. 12E), while others are made up of strongly folded horizons (Fig. 12F). Sand facies grades or alternate with greyish to dark fine sand and silt to clay that are generally finely laminated (Fig. 12A, C), except a few massive beds. F1 and F2 facies exhibit syn-sedimentary deformation shown by small syn-sedimentary faults and contorted beds.

4.3.1.2. Interpretation. Flat-pebble conglomerate results from the failure and subsequent ductile and brittle deformation of compacted to early cemented deposits (Myrow et al., 2004). Flat pebbles preserving angular shapes and laminated structure support limited transport, suggesting relatively proximal environments (Table 4). Failure of early cemented deposits can have been induced either by storm or seismic activity. The occurrence of disordered and chaotic horizons, rafted packages of sandstone and rip up mud clasts support the interpretation of flat-pebble conglomerate originating from the failure of loosely consolidated sediments along slide scars (Martinsen, 1994; Myrow et al., 2004). Such depositional process is also consistent with elutriation bands that are indicative of water escape from rapidly deposited sand (Lowe and LoPiccolo, 1974; Ravier et al., 2015). The interbedding of flat-pebble conglomerates and sandstone with fine-grained sediments indicates a deposition below the fair-weather wave base.

4.3.2. Facies association 5

4.3.2.1. Description. This association consists of tens of cm-to m-thick thinly laminated beds (Fig. 12G and H). These layers are made up of alternations of mm-thick magnetite layers with greyish to greenish layers made up of carbonates with minor clay and silt (C2, Table 3). From place to place, beds of facies C2 are faulted or folded and crosscut by calcite veins (Fig. 12G and H). Carbonate layers grade or alternate with siliciclastic layers corresponding either to S1 or F1 facies. S1 facies is made up of fine sand and is generally massive and sometimes comprise rip-up mud clasts. F1 facies is made up of silt to clay and exhibits horizontal laminations.

4.3.2.2. Interpretation. Facies association 5 is mainly made up of iron and carbonate-rich facies and occurs only toward the base of the drill core FD52. This association indicates periods of limited terrigenous input that allowed for the precipitation of carbonates and iron oxides (Table 4).

5. Geochronological constraints

Cathodoluminescence images of representative grains and analytical results are available in Appendices 2 and 3, respectively.

5.1. Carajás Formation

Although being collected in different lithologies (volcaniclastic basaltic sandstone, GIF), detrital zircon grains extracted from three different samples in drill-cores FD110 (*FD110 359.00-359.35*) and FD353 (*FD353 188.10-188.30* and *FD353 191.70-191.90*) exhibit similar characteristics. Most of the grains have euhedral shape and are pinkish, slightly to very elongated (length to width ratio of 2:1 to 10:1), and some contain small inclusions. Very few grains are sub-rounded. After TACA treatment, most of the grains were translucent and spotless, while a few remained pinkish with an etched surface. Most of the zircon crystals display a well-defined oscillatory zoning typical of magmatic zircon (Corfu et al., 2003), but some grains are not zoned or display a core-rim structure. The Th/U ratios of all concordant grains range between 0.32 and 3.44., also supporting a magmatic origin (Rubatto, 2002).

Most of the grains from the volcaniclastic sample *FD110 359.00-359.35* form a cluster giving a concordia date of 2719.6 ± 5.6 Ma (MSWD = 0.47, n = 35; Fig. 13; Table 5). In the sample *FD353 188.10-188.30*, the youngest cluster gives a concordia date of 2732.4 ± 5.2 Ma (MSWD = 0.53, n = 37; Fig. 13; Table 5). In the GIF sample *FD353 191.70-191.90*, concordant analyses give a date of 2728.5 ± 5.2 Ma (MSWD = 0.57, n = 38). These dates are interpreted as MDAs for these samples (Fig. 13; Table 5). Older concordant grains correspond to xenocrysts or epicrysts.

5.2. Igarapé Bahia Group

The detrital zircon grains collected in the Igarapé Bahia Group have diverse size, shapes (euhedral to rounded), and colors. Euhedral grains are translucent to pinkish and elongated. Rounded to sub-angular grains are reddish, yellowish, pinkish, or brownish, without apparent relationship between color and shape. Internal structures as well as Th/U ratios support a magmatic origin for all grains.

In the conglomerate *FD52 651.30-651.80*, the youngest cluster gives

Fig. 7. Syn-to post-depositional deformations, diagenetic and metamorphic features in the Carajás Formation. Arrows point to the stratigraphic top. Facies codes: Table 3. **A.** Sample FD55 351.90. Jaspilitic BIF comprising a late diagenetic inflated bed composed of magnetite with small veins rooted in the inflated bed (white triangles) crosscutting the underlying BIF. **B.** Sample FD354 242.20. Large secondary minerals in a jaspilitic BIF. **C.** Sample S11D214 449.00. Chert displaying folded layers and a few clasts, attesting for a ductile to brittle deformation attributed to slumping processes. **D.** Sample FD365 340.80. Highly contorted lamination in carbonate BIF resulting from the loading of dense Fe-rich layers onto carbonate beds. **E.** Sample FD365 262.20. Carbonate BIF showing intraformational angular clasts along a slip surface. Syn-sedimentary faults crosscut both intraformational clasts and carbonate BIF. Two erosion surfaces are present above the intraformational angular clasts. **F.** Sample S11D214 323.10. Injectite in black shales.

a concordia date of 2788 ± 12 Ma (n = 6, MSWD = 1.10), interpreted as a MDA (Fig. 13; Table 5). The youngest cluster of the sandstone *FD52 637.26-637.65* gives a concordia date of 2829 ± 17 Ma (n = 3, MSWD = 0.48). In samples *FD52 602.40-603.00* and *FD52 393.35-393.90*, the youngest clusters give concordia dates of 2753 ± 18 Ma (n = 3, MSWD = 0.44) and 2785 ± 16 Ma (n = 3, MSWD = 1.8), respectively, interpreted as MDAs (Fig. 13; Table 5). Other concordant dates spread from the MDAs up to the mid Mesoarchean. In samples *FD52 651.30-651.80* and *FD52 637.26-637.65* two grains yielded dates of 2666 ± 29 Ma and 2663 ± 27 Ma, respectively, the significance which is further discussed in the next section.

6. Discussion

6.1. Age of deposition and link with the parauapebas LIP

6.1.1. Carajás Formation

Volcaniclastic rocks of the Carajás Formation gave MDAs ranging from ca. 2732 to 2720 Ma (Fig. 13). This indicates that the Carajás Formation was deposited from 2751 ± 4 Ma (Krymsky et al., 2007) to at least 2720 ± 6 Ma (this work). This results in a range of age longer than the previously estimated stratigraphic range by ca. 20 Ma (Fig. 2; Table 1), indicating that BIFs were deposited during a long period of time (≥ca. 40 Myrs) in the Carajás Basin. Considering an average thickness of 250 m (Beisiegel et al., 1973; Lindenmayer et al., 2001) and a deposition period of 40 Myrs (that is a minimum estimate given that the results obtained in this study are maximum depositional ages), an accumulation rate of ca. 6 m.Ma^{-1} can be estimated. This value is in agreement with those already documented for IFs elsewhere (Arndt et al., 1991; Barton et al., 1994; Beukes and Gutzmer, 2008; Lantink et al., 2019; Simonson and Hassler, 1996).

The similarity between MDAs from the Carajás Formation and the age of emplacement of dolerite sills intruding it (e.g., Trendall et al., 1998) supports the contemporaneity of volcanism and sedimentation. The volcanic activity associated with the Parauapebas LIP thus lasted until ca. 2.72 Ga, while the earliest volcanic activity occurred at ca. 2.76 Ga (e.g., Machado et al., 1991) and the main peak in magmatic activity occurred at ca. 2.75 Ga (Fig. 3; Table 2). This suggests that the Parauapebas LIP had a total lifespan of ca. 40 Myrs, which is consistent with the duration of magmatism commonly observed for other LIPs elsewhere (Bryan and Ernst, 2008). The Parauapebas LIP comprises mainly mafic rocks (Lacasse et al., 2020), but also felsic units including rhyolites (Table 1). Thus, zircon grains from the Carajás Formation probably derived from such felsic volcanic rocks, although alkaline basalts from

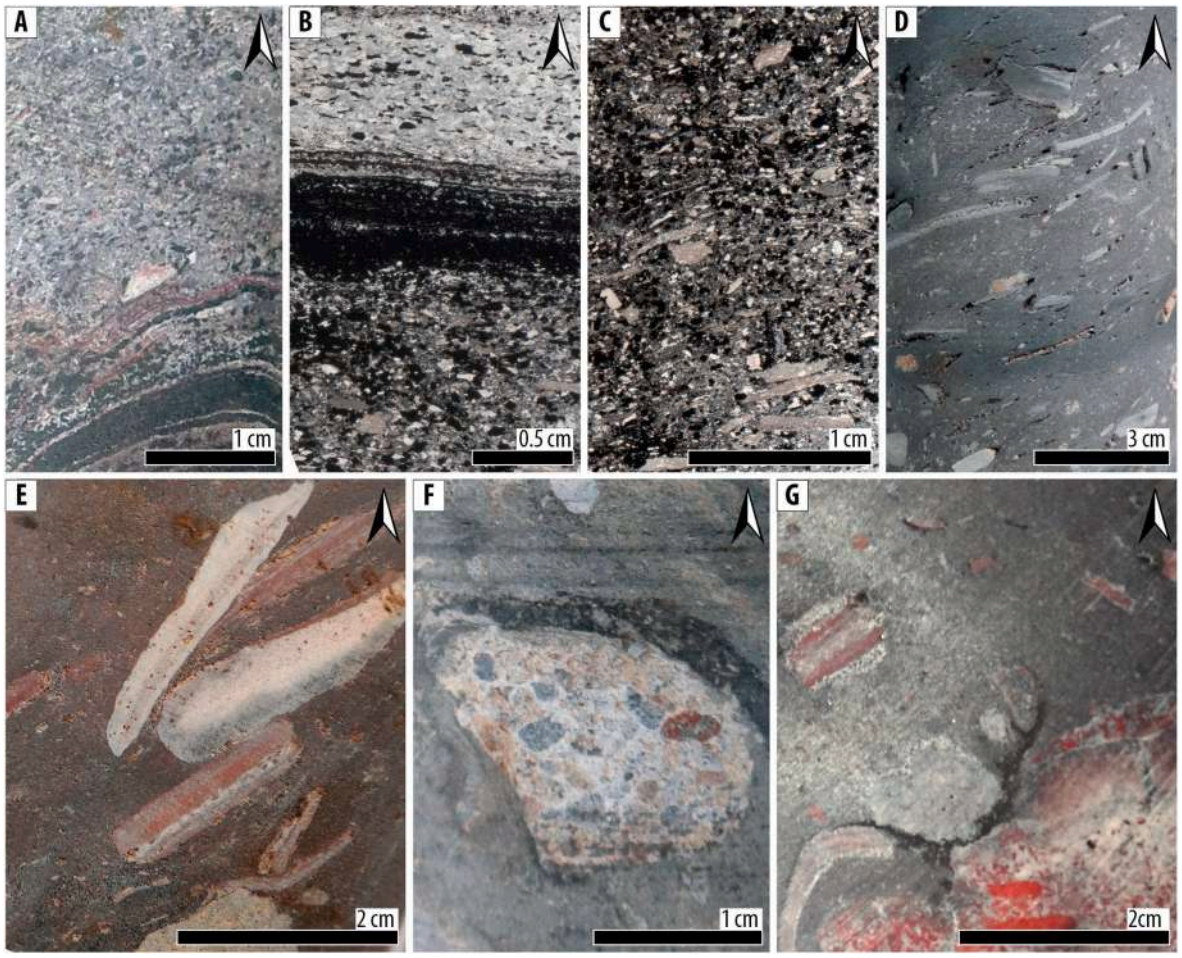

Fig. 8. Granular iron facies and conglomerates of the Carajás Formation. Arrows point to the stratigraphic top. **A.** Sample FD55 475.10. Granular Iron Formation (GIF) comprising very elongated, sub-angular to rounded chips with rounded ends and slight bending. The clasts are made up of chert and are flattened parallel to the bedding. **B.** Sample FD55 475.05. Thin section in reflected light showing interlayered GIFs and BIFs. **C.** Sample FD55 475.15. Thin section in reflected light showing chert clasts with rounded to very elongated shapes. The chert clasts are embedded within a cherty matrix comprising oxide minerals. Elongated clasts are flattened parallel to the bedding. **D.** Sample FD354 91.60. Monomictic matrix-supported conglomerate with elongated clasts. Most of the clasts are slightly bended. Fine-grained ferruginous matrix. Long axes of clasts show a preferred orientation. **E.** Sample S11D214 494.00. Matrix-supported conglomerate with elongated chert clasts in a very fine ferruginous matrix. The clasts exhibit a preferred orientation and rounded to sub-rounded ends. **F.** Sample S11D214 339.50. Clast made up of coarse sandstone. **G.** Sample S11D214 487.30. Conglomerate displaying rounded to sub-rounded clasts as well as bended and elongated chert clast.

the Parauapebas LIP are also zircon-rich (Martins et al., 2017) and may also have represented a source for the volcaniclastic rocks of the Carajás Formation.

6.1.2. *Igarapé Bahia Group*

In contrast with the Carajás Formation, no volcaniclasts have been identified in the Igarapé Bahia Group (drill-core FD52; cf. section 4.3), and MDAs are not getting younger upward (Fig. 13), suggesting that there was no active volcanism during the deposition of the Igarapé Bahia Group. The two youngest grains from the Igarapé Bahia Group (2666 ± 29 Ma and 2663 ± 27 Ma) exhibit well-defined oscillatory zoning, suggesting a magmatic origin for these grains (cf. Appendix 2). If no lead loss occurred, the concordia date of this youngest cluster (2664 ± 32 Ma, n = 2, MSWD = 0.03) may thus represents the MDA of the Igarapé Bahia Group. Although this age should be considered as provisional as ancient lead loss cannot be ruled out, it suggests that Igarapé Bahia Group was deposited between ca. 2.7 and 2.6 Ga (Perelló et al., 2023; Requia et al., 2003; Tallarico et al., 2005).

6.2. *Evolution of depositional environments associated with the emplacement of the parauapebas LIP*

The typical amygdaloidal texture of the Parauapebas basalts indicates a low confining pressure (Fig. 4A and B) and is commonly observed in subaerial (Liebmann et al., 2022) and low-depth submarine basalts (Dann, 2001; Merle et al., 2005). This is consistent with the presence of microbially induced sedimentary structures (MISS) suggesting shallow water depositional environments in the photic zone soon after the emplacement of the Parauapebas Fm (Fig. 5). Carbonate rich-BIFs could be an indirect evidence of high productivity in surface waters (Heimann et al., 2010), echoing previous observations of bacterial activity (Rego et al., 2021; Ribeiro da Luz and Crowley, 2012). Together, these observations highlight environmental conditions favorable for life development. Facies associations 1 and 2 correspond to deeper environments, probably below wave base (Fig. 14A). The occurrence of extreme positive europium anomalies in IFs from the Carajás Fm. suggests that Fe mainly originates from hydrothermal fluids (Rego et al., 2021). The mafic composition of the Parauapebas LIP (Lacasse et al., 2020) and the contemporaneity between volcanism and the deposition of IFs of the Carajás Formation further argue for a local hydrothermally-derived Fe source linked with the emplacement of the

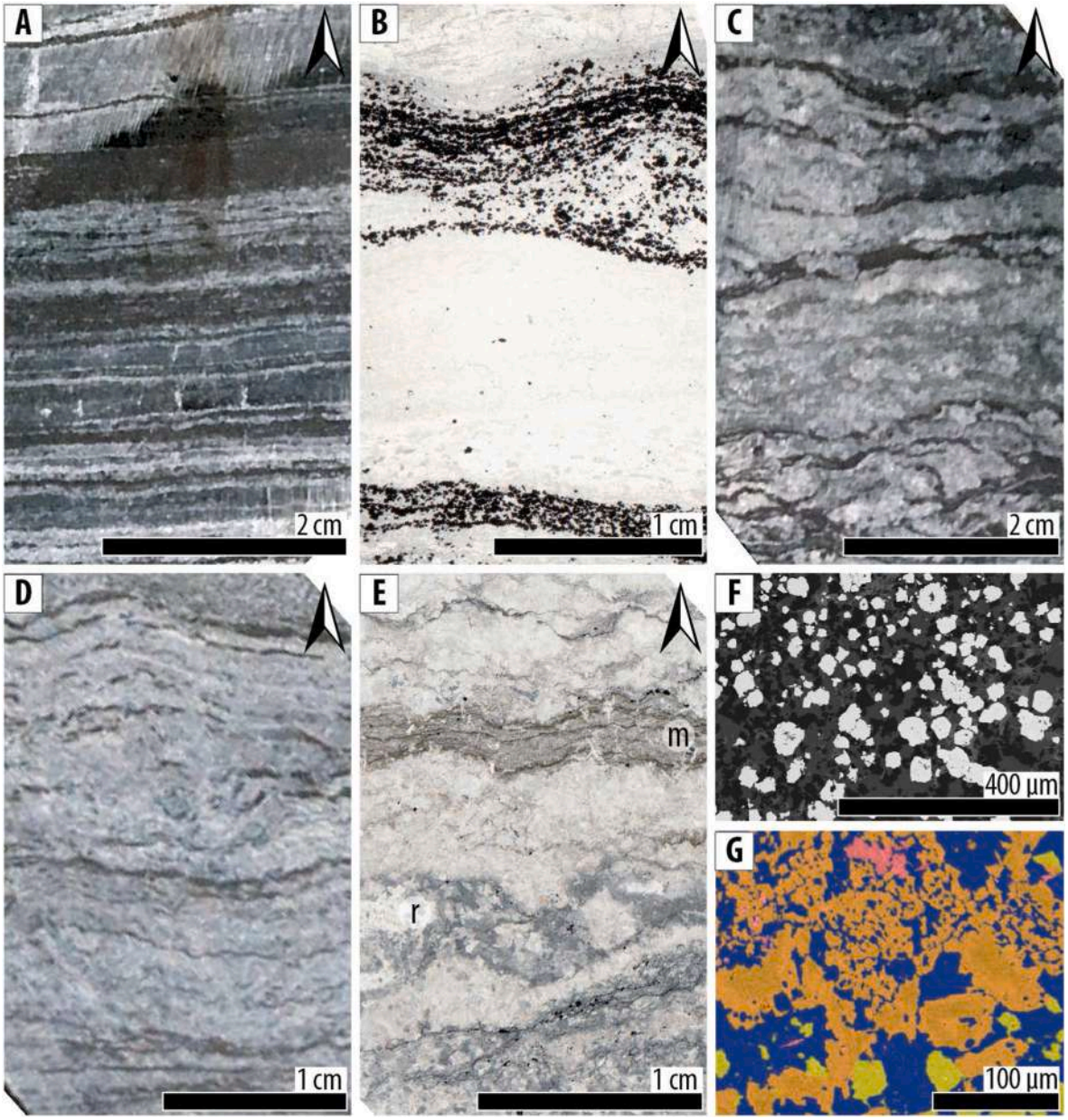

Fig. 9. Carbonate facies of the Carajás Formation. Arrows point to the stratigraphic top. **A.** Sample FD55 521.60. Fine laminations of Fe-bearing minerals (mainly magnetite) and carbonate layers. **B.** Sample FD55 521.12. Thin section in reflected light showing wavy laminations underlined by magnetite grains and carbonates. **C.** Sample FD55 518.50. Carbonate with irregular, crinkled magnetite laminations and pinching out geometries. **D.** Sample FD55 522.56. Carbonate with very fine, crinkled lamination underlined by very fine magnetite layers. **E.** Sample FD55 520.06. Thin section in reflected light showing a microbial mat (m) within carbonate displaying a clotted micritic texture. Some areas show recrystallized (r) textures. **F.** Sample FD55 514.57. Electron backscattered image showing diagenetic framboidal pyrite (bright white) minerals within a carbonate matrix. **G.** Sample FD55 514.57. EDS electron image showing Si, Ca and Fe-rich mineral phases. Calcite appears in green, ankerite in orange, chert in dark blue, and magnetite in pink.

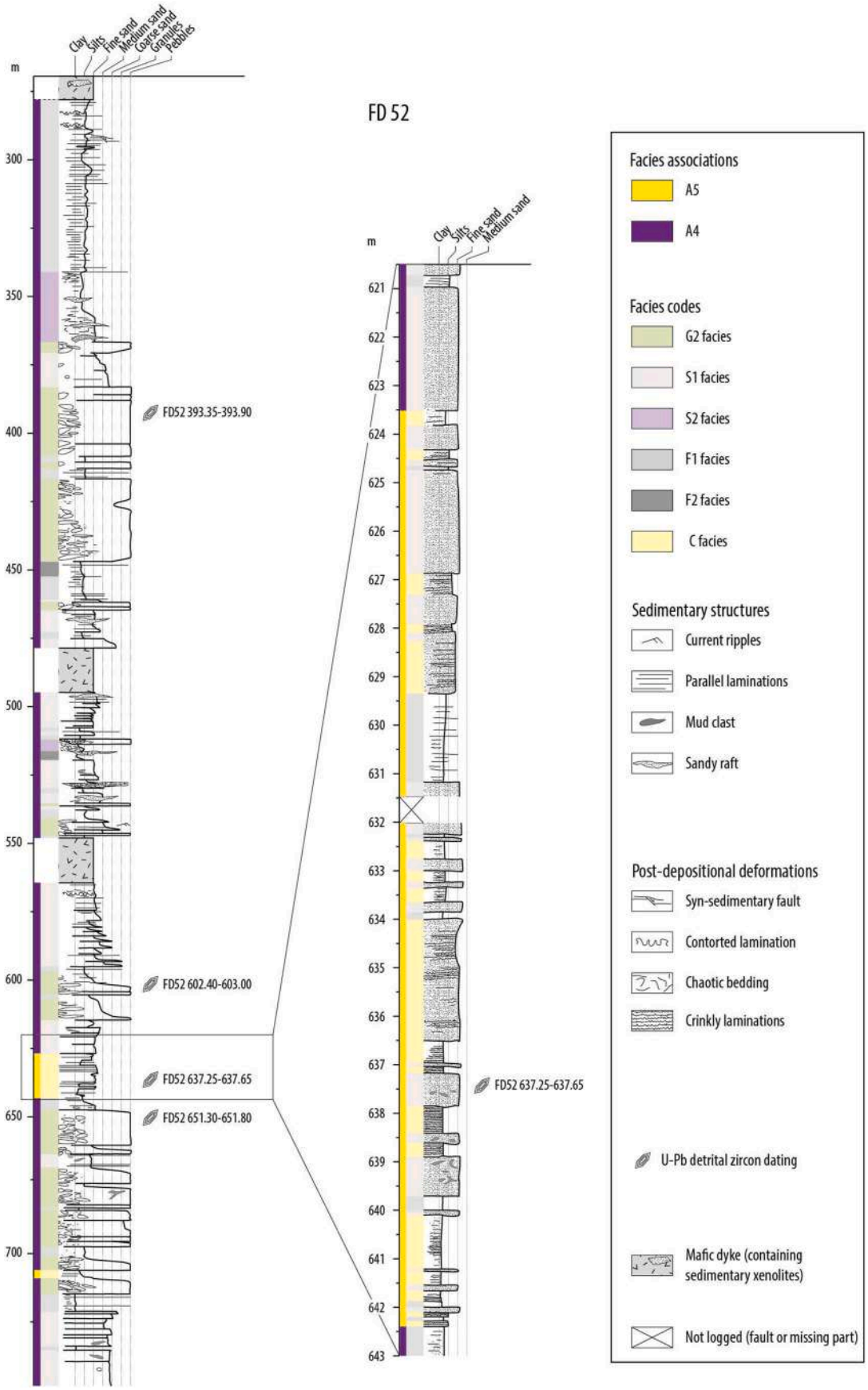

Fig. 10. Sedimentological log of the drill core intersecting the Igarapé Bahia Group. Facies codes: Table 3. Facies association: Table 4. The upper part of the drill core intercepts another formation (Appendix 1).

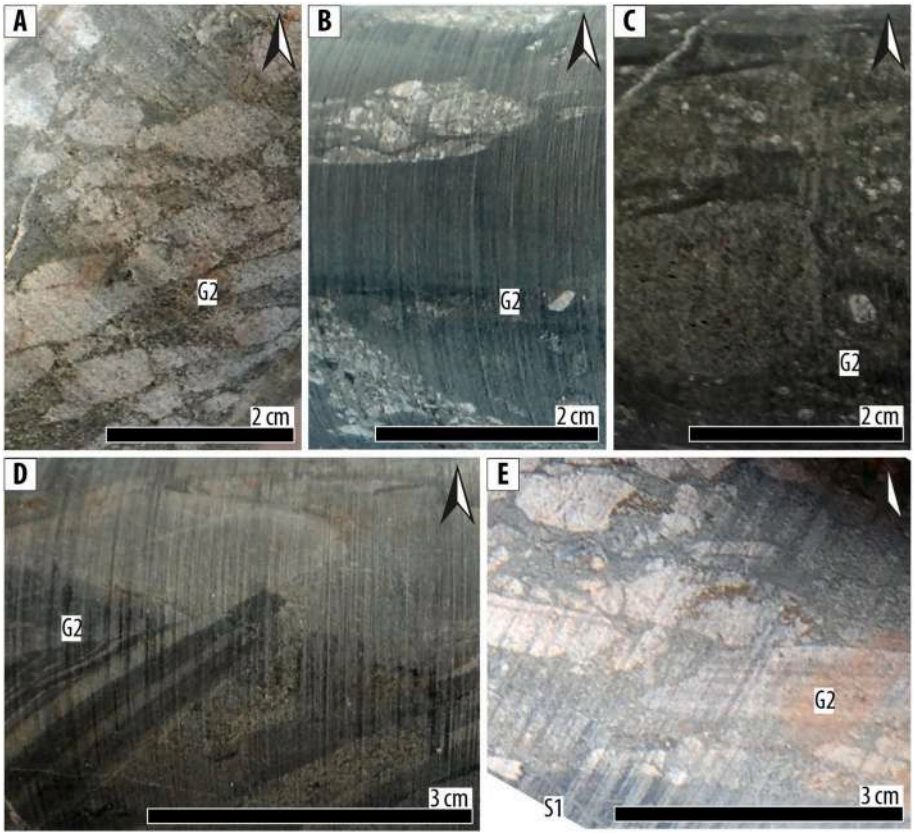

Fig. 11. Conglomerate facies from the Igarapé Bahia Group. Arrows point to the stratigraphic top. Facies codes: Table 3. **A.** Sample FD52 546.50. Flat-pebble conglomerate made up of elongated, sub-angular to sub-rounded clasts embedded within a greenish matrix. Most of the clasts are sandy, a few clasts are muddy. **B.** Sample FD52 530.60. Flat-pebble conglomerate comprising sandy clasts embedded into a muddy to silty matrix. **C.** Sample FD52 392.65. Flat-pebble conglomerate, comprising mainly muddy clasts, sandy clasts and mixed clasts preserving original sedimentary structure. **D.** Sample FD52 441.85. Flat-pebble conglomerate, clasts supported. Some clasts preserve a sedimentary bedding. Occurrence of muddy clasts, sandy clasts and mixed clasts preserving original sedimentary structure. **E.** Sample FD52 536.49. Flat-pebble conglomerate comprising sandy clasts flattened parallel to the bedding. The contact with the underlying fine sandstone to siltstone is sharp and non-erosive.

Parauapebas LIP (Fig. 15A and B).

Facies associations of the Igarapé Bahia Group are indicative of offshore settings (Fig. 14B). Regarding IFs at the base of the Igarapé Bahia Group, an external iron source could be involved in their formation given their contemporaneity with a period of enhanced mafic magmatic activity worldwide (Fig. 15C; Abbott and Isley, 2002; Isley and Abbott, 1999). Nonetheless, the persistence of IFs deposition in the Carajás Basin could also be indicative of sustained hydrothermal activity by the Paraupebas LIP long after the end of magmatic activity.

The transition from a chemically-to a terrigenous-dominated sedimentary system indicates that a significant environmental change occurred during the deposition of the Carajás IFs and the Igarapé Bahia Group. This transition may be related to a relative sea-level drop that promoted inland erosion and generated an influx of terrigenous materials into the basin, as reported elsewhere (e.g., Simonson and Hassler, 1996). Deposits from the Igarapé Bahia Group are closely associated with major faults (Fig. 1C), and comprise numerous soft sediment deformations structures potentially indicative of an active tectonic setting (Rossignol et al., 2020) that could have triggered or enhanced the influx of terrigenous material in the basin (Fig. 15D). This concurs with the report of tectonic activity that reactivated Mesoarchean structures at ca. 2.75 to 2.73 Ga, either related to transpressional strike-slip shear zones (Marangoanha et al., 2019a; Silva et al., 2020) or to the formation of an active rift basin (Feio et al., 2012; Martins et al., 2017; Olszewski et al., 1989; Tavares et al., 2018; Toledo et al., 2019). The influx of terrigenous material can also have been promoted by the emergence of the Amazonia Craton during a period of large-scale emersion of terrestrial areas (Fig. 15E; e.g., Liebmann et al., 2022).

6.3. Relationships with neoarchean paleoenvironmental changes

The newly defined age range for the deposition of the Carajás IFs show that they are contemporaneous with numerous other IFs that have been deposited in distinct paleogeographic locations between ca. 2.75 Ga to 2.70 Ga, in the Yilgarn, Tanzanian, Dharwar, Rae, Zimbabwe, Karelia, Congo and Superior cratons (Fig. 15F). Similarly to the Carajás IFs, most of these 2.75–2.70 Ga IFs are closely associated with mafic magmatic rocks (although not always characterized as LIPs), pointing to significantly high mantle input of hydrothermally-derived iron into seawater at that time (Barley et al., 1997; Isley, 1995; Isley and Abbott, 1999; Viehmann et al., 2015).

Considering an average density of $3.48{\cdot}10^{6}$ g m^{-3} (Konhauser et al., 2018), an accumulation rate of 6 m.Myr^{-1} (compacted sediments), a deposition period of ca. 40 Myrs and a basin dimension $\geq 1.8{\cdot}10^{10}$ m^{2}, we calculated that more than 15,000 Gt (giga tons) of IFs were deposited in the Carajás Basin. This quantification should be considered as preliminary given that the accumulation rate and the size of the basin are rough estimates. Despite these uncertainties, our quantification gives a first order estimate of the quantity of IFs deposited in the Carajás Basin. This agrees with previous studies, which estimated a total mass of IFs between 10,000 and 50,000 Gt for the same location (e.g., Konhauser et al., 2017). Moreover, the sediment accumulation rate derived from our geochronological results allow to assess the rate of Fe accumulation normalized per unit area and compare it with other IF deposits elsewhere. Considering the average Fe_2O_3 content of Carajás IFs (56.2 wt%; Rego et al., 2023) gives a Fe flux of 8 g $m^{-2}.y^{-1}$ (or 0.15 mol $m^{-2}.y^{-1}$) in the Carajás Basin. In the Hamersley Basin, where IF deposition is also assumed to be coeval with subaerial LIP emplacement (Barley et al., 1997; Isley and Abbott, 1999), observed accumulation rates for chemical sediments range between 3 and 15 m.Myr^{-1} (Arndt et al., 1991; Lantink, 2022) resulting in a net Fe flux comprised between 4 and 22 g $m^{-2}.y^{-1}$. This indicates that the Fe flux estimated for the Carajás Basin compares well with those of other large IFs deposits related to LIP emplacement.

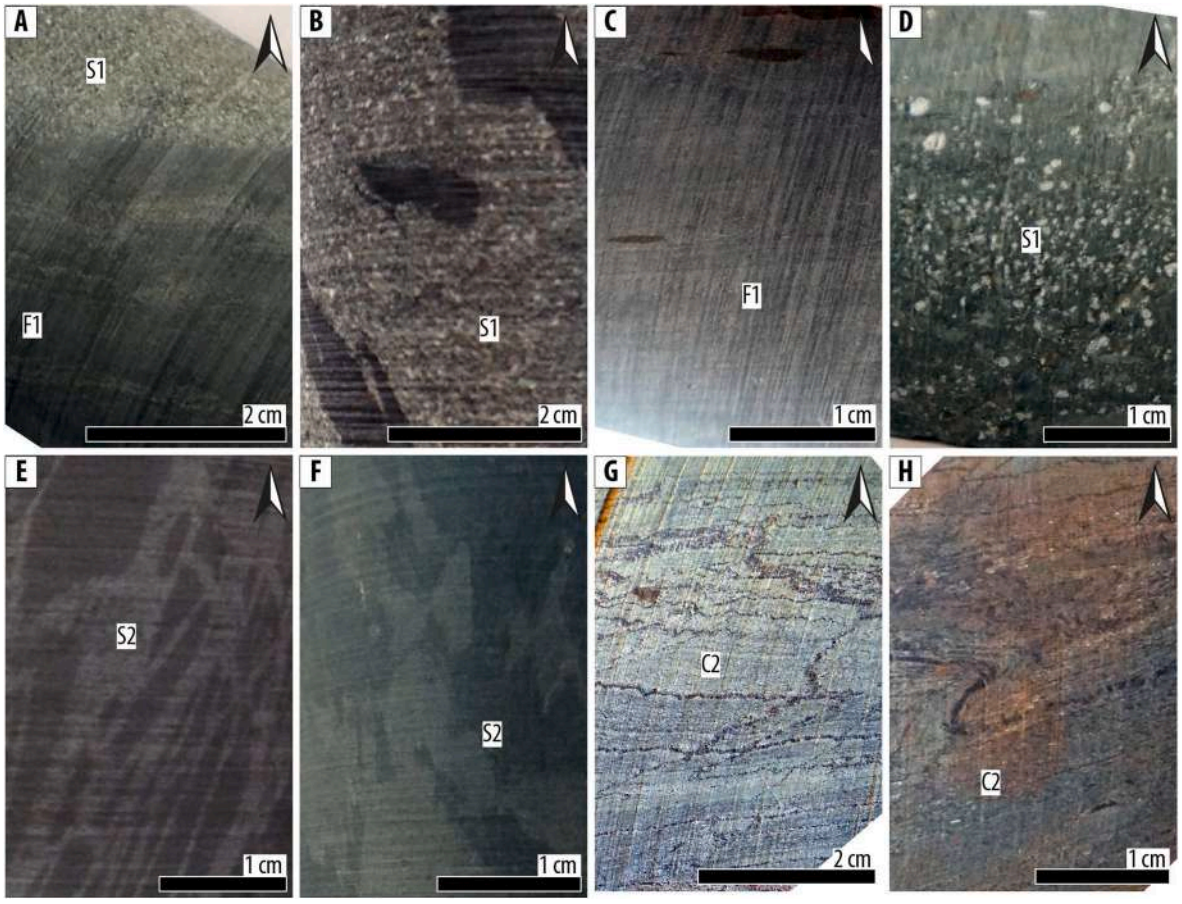

Fig. 12. Sandstone, siltstone and carbonate facies from the Igarapé Bahia Group. Arrows point to the stratigraphic top. Facies codes: Table 3. **A.** Sample FD52 471.20. F1 facies with planar lamination underlined by fine sandstone layers grading to S1 facies. **B.** Sample FD52 618.80. S1 facies containing mud clasts. **C.** Sample FD52 320.30. F1 facies with fine horizontal laminations. **D.** Sample FD52 423.00. Fine sandstone to siltstone containing a "raft" made up of coarse sand embedded within a muddy matrix. **E.** Sample FD52 515.80. Anastomosed elutriation bands. **F.** Sample FD52 355.40. Strongly folded sandstone to siltstone horizon, where initial bedding planes are not recognizable. **G.** Sample FD52 636.60. Thinly laminated greenish carbonate alternating with millimetric magnetite layers. Post-depositional micro-folding. **H.** Sample FD52 623.60. Greenish carbonate beds alternating with millimetric magnetite layers. Post-depositional folds and calcite veins.

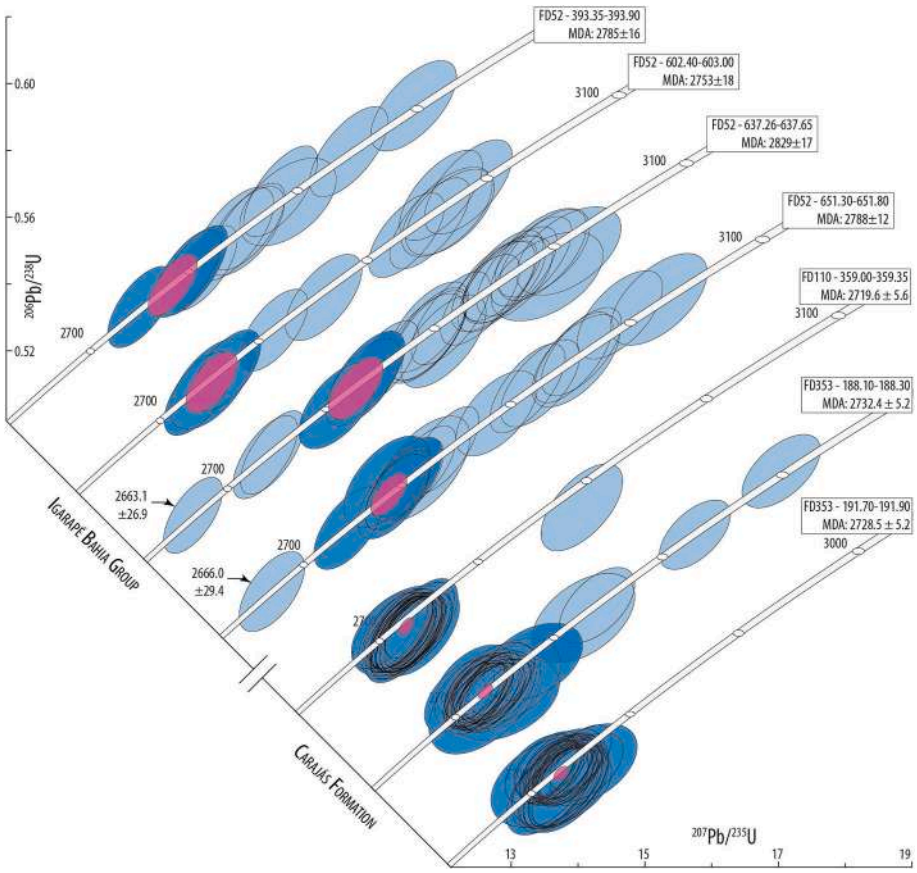

Fig. 13. Wetherill concordia diagrams. Error ellipses are depicted at the 2σ level. **A.** Analyses used to calculate the Maximum Depositional Age (MDA) are depicted in dark blue. Other concordant analyses are depicted by pale blue. The weighted mean error ellipse (concordia date) of the youngest cluster of concordant grains is depicted in pink. The number of analyses, the mean square weighted deviate for concordance and equivalence and the probability for concordance and equivalence for each MDA are provided in Table 4. **B.** MDA calculated from the youngest grains of four samples from the Igarapé Bahia Group, assuming the grains are cogenetic in origin. N_a: number of analyses; N_{zrc}: number of zircon grains; MSWD: Mean Square Weighted Deviate for concordance and equivalence; Prob.: probability for concordance and equivalence.

Table 5
Summary of maximum depositional ages.

Sample	N_{zr}	Probability of concordance ≥10%, decay constants errors included								
		Detection limits (%)				Maximum depositional age				
		$DL_{1(pL = 0.5)}$	$DL_{1(pL = 0.95)}$	$DL_{3(pL = 0.5)}$	$DL_{3(pL = 0.95)}$	Concordia age	± (2σ)	n	MSWD	Probability
Carajás Formation										
FD110–359.00–359.35	36	1.9	8.0	7.4	16.5	2719.6	5.6	35	0.47	1.00
FD353–188.10–188.30	41	1.7	7.0	6.5	14.6	2732.4	5.2	37	0.53	1.00
FD353–191.70–191.90	38	1.8	7.6	7.0	15.7	2728.5	5.2	38	0.57	1.00
Igarapé Bahia Group										
FD52–393.35–393.90	11	6.3	23.8	23.6	47.1	2785	16	3	1.8	0.11
FD52–602.40–603.00	11	6.3	23.8	23.6	47.1	2753	18	3	0.44	0.82
FD52–637.26–637.65	25	2.7	11.3	10.6	23.2	2829	17	3	0.48	0.79
FD52–651.30–651.80	19	3.6	14.6	13.9	29.6	2788	12	6	1.10	0.36

N_{zr}: number of concordant zircon grain analyzed per sample; n: number of analyses used to calculate the maximum deposition age; DL: detection limit, calculated after Rossignol et al. (2019); DL_1: detection limit for at least one grain; DL_3: detection limit for at least three grains; $_{pL}$: probability level assigned to the detection limits; MSWD: mean square of weighted deviates. The MSWD and the probability given for the concordia ages are for both concordance and equivalence; na: non applicable.

7. Conclusions

The deposition of IFs in the Carajás Basin is related to the emplacement of the Parauapebas LIP, which exerted a strong influence on depositional environments both in space and time. The Parauapebas LIP controlled environments at the basin-scale by releasing a large amount of iron in seawater through hydrothermal activity. This in turn favored the deposition of IFs in a variety of depositional settings, ranging from shallow to deep-water environments. Most of the IFs from the Carajás Basin have been deposited during the waning volcanic activity of the Parauapebas LIP, during a prolonged period of time that exceeded 30 Myrs. Although of lower intensity, the impact of the Paraupebas LIP on nearby depositional environments could even have lasted longer, as suggested by the occurrence of IFs in the overlying Igarapé Bahia Group.

The long-lasting control on depositional environments exerted by the Parauapebas LIP also suggests that the LIP could have impacted biogeochemical cycles, at least at the basin-scale. The release of large amounts of solutes and soluble Fe over a significant period of time likely contributed to enhance photoferrotrophic microbial metabolism in surface waters as recently documented by Rego et al. (2021).

CRediT authorship contribution statement

Camille Rossignol: Writing – original draft, Visualization, Methodology, Investigation, Formal analysis, Conceptualization. **Eric Siciliano Rego:** Writing – review & editing, Investigation, Formal analysis, Conceptualization. **Pascal Philippot:** Writing – review & editing, Supervision, Project administration, Investigation, Funding acquisition,

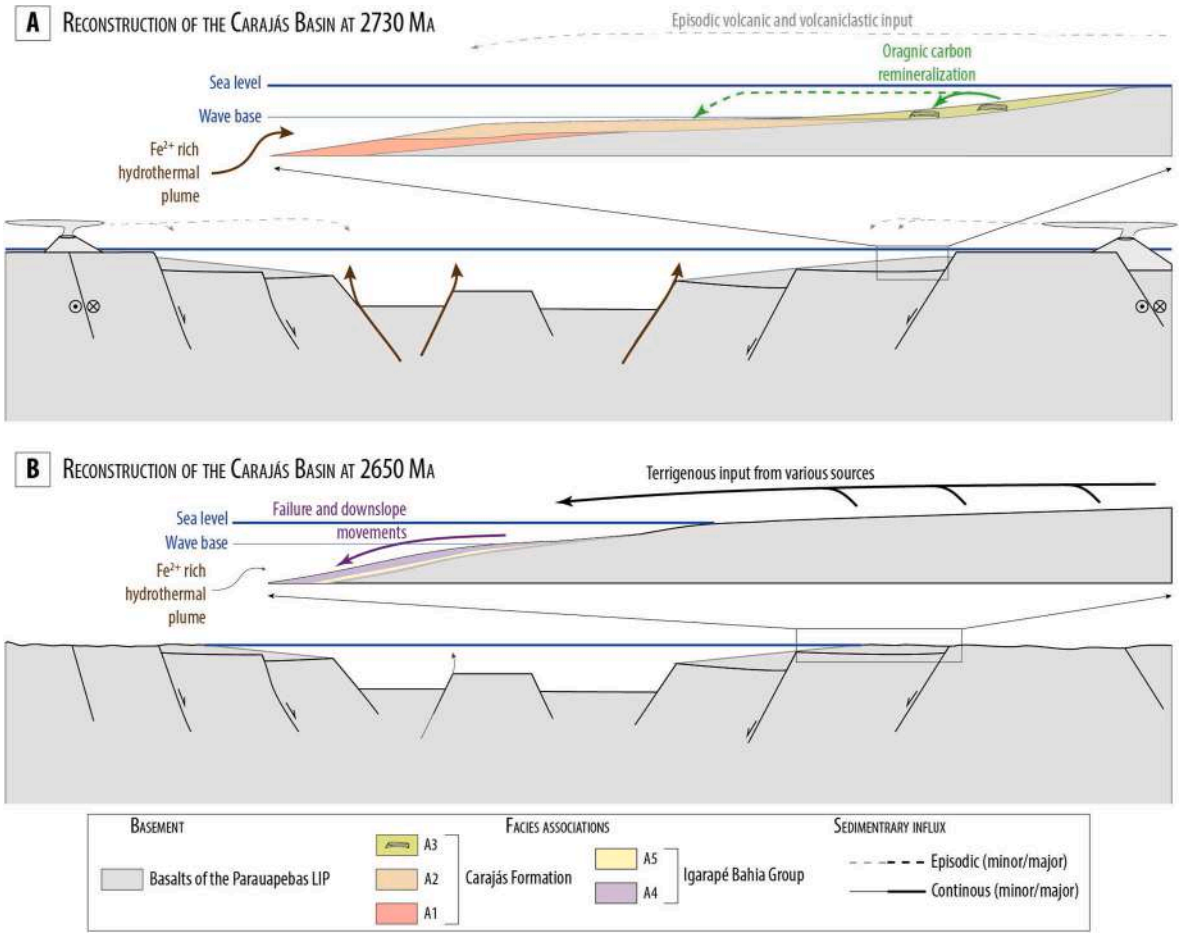

Fig. 14. Schematic cross-sections of the Carajás Basin during the Neoarchean. **A.** Paleoenvironmental and tectonic settings of the Carajás Basin during the deposition of the Carajás Formation, at ca. 2730 Ma. **B.** Paleoenvironmental and tectonic settings of the Carajás Basin during the deposition of the Igarapé Bahia Group at ca. 2650 Ma.

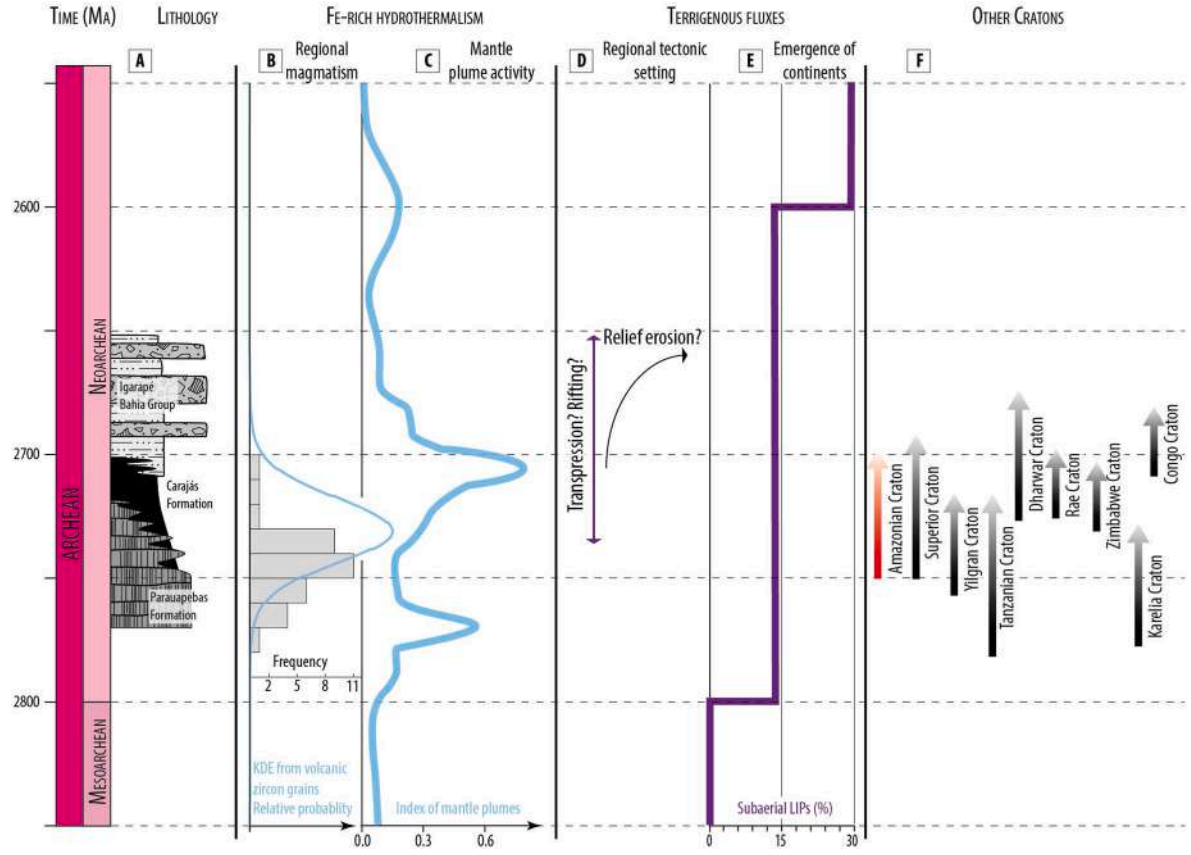

Fig. 15. Chart summarizing the main characteristics of the Carajás Formation and Igarapé Bahia Group and their relationships with regional and global Neoarchean geodynamic events. **A.** Synthetic lithostratigraphy. **B.** Index of volcanic activity from the age distribution of concordant zircon grains of the Carajás Formation. Histogram: frequency distribution of zircon U–Pb dates of rocks from the Parauapebas Large Igneous Province (Fig. 2). KDE: Kernel Density Estimator (bandwidth = 15) for the Carajás Formation, based on TACA and untreated grains (Appendix 3). **C.** Index of mantle plume activity (after Abbott and Isley, 2002). **D.** Regional tectonic setting (Feio et al., 2012; Martins et al., 2017; Olszewski et al., 1989; Tavares et al., 2018; Toledo et al., 2019). **E.** Proportion of subaerial LIPs (Liebmann et al., 2022). **F.** Comparison of the age of IFs deposits in the Amazonia and in the Yilgarn (Wilgie Mia Formation; Czaja et al., 2018), Tanzanian (Upper Nyanzian Group; Kwelwa et al., 2018), Dharwar (Mulaingiri Formation; Sunder Raju and Mazumder, 2020), Rae (Mary River Group; Bros and Johnston, 2017; Jackson et al., 1990), Zimbabwe (Tati Greenstone Belt; Døssing et al., 2009), Karelia (Gimoloy Group; Slabunov et al., 2021), Congo (Nyong Unit; Chombong et al., 2017), and Superior cratons (Temagami Greenstone Belt, Michipicoten Group; Bowins and Heaman, 1991).

Conceptualization. **Francesco Narduzzi:** Writing – review & editing, Investigation. **Lívia Teixeira:** Writing – review & editing, Investigation. **Marco A.L. Silva:** Writing – review & editing, Data curation. **Janaína N. Ávila:** Writing – review & editing, Investigation. **Cristiano Lana:** Writing – review & editing, Resources, Methodology, Investigation, Formal analysis, Data curation. **Ricardo F. Trindade:** Funding acquisition.

Declaration of competing interest

The authors declare the following financial interests/personal relationships which may be considered as potential competing interests: Camille Rossignol reports financial support was provided by Fundação Amparo à Pesquisa do Estado de São Paulo. Cristiano Lana reports financial support was provided by Conselho Nacional de Desenvolvimento Científico e Tecnológico. Cristiano Lana reports was provided by Fundação Amparo à Pesquisa do Minas Gerais. Eric Siciliano Rego reports financial support was provided by Fundação Amparo à Pesquisa do Estado de São Paulo. Pascal Philippot reports financial support was provided by Fundação Amparo à Pesquisa do Estado de São Paulo. Francesco Narduzzi reports financial support was provided by Fundação Amparo à Pesquisa do Estado de São Paulo. Livia Teixeira reports financial support was provided by Fundação Amparo à Pesquisa do Estado de São Paulo. Ricardo F. Trindade reports financial support was provided by Fundação Amparo à Pesquisa do Estado de São Paulo.

Data availability

Supplementary information is archived at the Pangea data repository at https://doi.org/10.1594/PANGAEA.931156.

Acknowledgements

This research was funded by grants of the Fundação de Amparo à Pesquisa do Estado de São Paulo (FAPESP; 2015/16235-2, 2018/02645-2, 2018/14617-3, 2018/05892-0, 2019/17732-0, 2019/16066-7, 2019/16271-0, 2019/12132-5, 2021/10949-4), the Conselho Nacional de Desenvolvimento Científico e Tecnológico (CNPq; 308045/2013-0 and 307353/2019-2), and the Fundação de Amparo à Pesquisa do Minas Gerais (FAPEMIG; project APQ-03793-16). We acknowledge Adriana de Cássia Zapparoli, formerly at Vale company, for her help to access the Vale's drill core library in Carajás. J. Pereira, D. Vasconcelos, A. Mazoz and A. R. Alkmim are acknowledged for assistance during sample preparation, CL imaging (Microscopy and Microanalysis Network of Minas Gerais), and data acquisition. Constructive comments by various reviewers on earlier versions helped to improve this manuscript. We thank V. Oliveros for editorial handling and F. Corfu and an anonymous reviewer for their comments and suggestions that improved the quality of this manuscript.

Appendix A. Supplementary data

Supplementary data to this article can be found online at https://doi.org/10.1016/j.jsames.2023.104574.

References

Abbott, D.H., Isley, A.E., 2002. The intensity, occurrence, and duration of superplume events and eras over geological time. J. Geodyn. 34, 265–307. https://doi.org/10.1016/S0264-3707(02)00024-8.

Almeida, J.A.C., Dall'Agnol, R., Leite, A.A.S., 2013. Geochemistry and zircon geochronology of the Archean granite suites of the Rio Maria granite-greenstone terrane, Carajás Province, Brazil. J. South Am. Earth Sci. 42, 103–126. https://doi.org/10.1016/j.jsames.2012.10.008.

Antonio, P.Y.J., D'Agrella-Filho, M.S., Nédélec, A., Poujol, M., Sanchez, C., Dantas, E.L., Dall'Agnol, R., Teixeira, M.F.B., Proietti, A., Martínez Dopico, C.I., Oliveira, D.C., Silva, F.F., Marangoanha, B., Trindade, R.I.F., 2021. New constraints for paleogeographic reconstructions at ca. 1.88 Ga from geochronology and paleomagnetism of the Carajás dyke swarm (eastern Amazonia). Precambrian Res. 353 https://doi.org/10.1016/j.precamres.2020.106039.

Antonio, P.Y.J., D'Agrella-Filho, M.S., Trindade, R.I.F., Nédélec, A., de Oliveira, D.C., da Silva, F.F., Roverato, M., Lana, C., 2017. Turmoil before the boring billion: paleomagnetism of the 1880–1860 Ma Uatumã event in the amazonian craton. Gondwana Res. 49, 106–129. https://doi.org/10.1016/j.gr.2017.05.006.

Araújo, R., Araújo Filho, R.C., Costa, L., 2021. Tectono-sedimentary evolution of the Paleoproterozoic succession of the Carajás Basin, southeastern Amazonian Craton, Brazil: insights from sedimentology, stratigraphy, and U–Pb detrital zircon geochronology. Precambrian Res. 362, 106290 https://doi.org/10.1016/j.precamres.2021.106290.

Arndt, N.T., Nelson, D.R., Compston, W., Trendall, A.F., Thorne, A.M., 1991. The age of the Fortescue Group, Hamersley Basin, Western Australia, from ion microprobe zircon U-Pb results. Aust. J. Earth Sci. 38, 261–281. https://doi.org/10.1080/08120099108727971.

Barley, M.E., Pickard, A.L., Sylvester, P.J., 1997. Emplacement of a large igneous province as a possible cause of banded iron formation 2.45 billion years ago. Nature 385, 55–58.

Barton, E.S., Altermann, W., Williams, I.S., Smith, C.B., 1994. U-Pb zircon age for a tuff in the Campbell Group, Griqualand West sequence, South Africa: implications for early Proterozoic rock accumulation rates. Geology 22, 343–346. https://doi.org/10.1130/0091-7613(1994)022<0343:UPZAFA>2.3.CO;2.

Beisiegel, V.D.R., Bernardelli, A.L., Drummond, N.F., Ruff, A.W., Tremaine, J.W.R., 1973. Geologia e Recursos Minerais da Serra dos Carajás. Rev. Bras. Geociencias 3, 215–242.

Beukes, N.J., 1983. Palaeoenvironmental setting of iron-formations in the depositional basin of the Transvaal Supergroup, South Africa. Dev. Precambrian Geol. 6, 131–142. https://doi.org/10.1016/S0166-2635(08)70043-4.

Beukes, N.J., Gutzmer, J., 2008. Origin and paleoenvironmental significance of major iron formations at the archean-paleoproterozoic boundary. In: Hagemann, S., Rosière, C.A., Gutzmer, J., Beukes, N.J. (Eds.), Banded Iron Formation-Related High-Grade Iron Ore. Society of Economic Geologists, pp. 5–47. https://doi.org/10.5382/Rev.15.01.

Borba, M.L., Tassinari, C.C.G., Matos, F.M.V., Sato, K., Huhn, S., Ferreira, S.N., Medeiros, C.A., 2021. Tracking hydrothermal events using zircon REE geochemistry from the Carajás Mineral Province, Brazil. J. Geochem. Explor. 221, 106679. https://doi.org/10.1016/j.gexplo.2020.106679.

Bowins, R.J., Heaman, L.M., 1991. Age and timing of igneous activity in the Temagami Greenstone Belt, Ontario: a preliminary report. Can. J. Earth Sci. 28, 1873–1876. https://doi.org/10.1139/e91-167.

Bros, E.R., Johnston, S.T., 2017. Field observations of the Mary River Group south of Tay Sound, northern Baffin Island, Nunavut: stratigraphy and structure of supracrustal sequences and surrounding plutonic units. Summ. Act. 2017 Canada-Nuvanut Geosci. Off. 69–80.

Bryan, S.E., Ernst, R.E., 2008. Revised definition of large igneous provinces (LIPs). Earth Sci. Rev. 86, 175–202. https://doi.org/10.1016/j.earscirev.2007.08.008.

Cabral, A.R., Bühn, B., Seabra Gomes, A.A., Galbiatti, H.F., Lehmann, B., Halder, S., 2017. Multiple sulfur isotopes from the Neoarchaean Serra Sul black shale, Carajás mineral province, northern Brazil. J. South Am. Earth Sci. 79, 377–383. https://doi.org/10.1016/j.jsames.2017.08.002.

Chombong, N.N., Suh, C.E., Lehmann, B., Vishiti, A., Ilouga, D.C., Shemang, E.M., Tantoh, B.S., Kedia, A.C., 2017. Host rock geochemistry, texture and chemical composition of magnetite in iron ore in the Neoarchaean Nyong unit in southern Cameroon. Trans. Institutions Min. Metall. Sect. B Appl. Earth Sci. 126, 129–145. https://doi.org/10.1080/03717453.2017.1345507.

Cordani, U.G., Ramos, V.A., Fraga, L.M., Cegarra, M., Delgado, I., de Souza, K.G., Gomes, F.E.M., Schobbenhaus, C., 2016. Tectonic Map of South America at 1:5.9M. Scale 1 5 900 000 CGMW-CPRM-.

Corfu, F., Hanchar, J.M., Hoskin, P.W.O., Kinny, P., 2003. Atlas of zircon textures. In: Hanchar, J.M., Hoskin, P.W.O. (Eds.), Zircon. Mineralogical Society of America and Geochemical Society, Washington, DC, United States, pp. 469–500.

Craddock, P.R., Dauphas, N., 2011. Iron and carbon isotope evidence for microbial iron respiration throughout the Archean. Earth Planet Sci. Lett. 303, 121–132. https://doi.org/10.1016/j.epsl.2010.12.045.

Czaja, A.D., Van Kranendonk, M.J., Beard, B.L., Johnson, C.M., 2018. A multistage origin for Neoarchean layered hematite-magnetite iron formation from the Weld Range, Yilgarn Craton, Western Australia. Chem. Geol. 488, 125–137. https://doi.org/10.1016/j.chemgeo.2018.04.019.

Dalstra, H., Guedes, S., 2004. Giant hydrothermal hematite deposits with Mg-Fe metasomatism: a comparison of the Carajás, Hamersley, and other iron ores. Econ. Geol. 99, 1793–1800. https://doi.org/10.2113/gsecongeo.99.8.1793.

Dann, J.C., 2001. Vesicular komatiites, 3.5-Ga komati formation, barberton greenstone belt, South Africa: inflation of submarine lavas and origin of spinifex zones. Bull. Volcanol. 63, 462–481. https://doi.org/10.1007/s004450100164.

Dimroth, E., 1975. Paleo-environment of iron-rich sedimentary rocks. Geol. Rundsch. 64, 751–767. https://doi.org/10.1007/BF01820694.

Døssing, L.N., Frei, R., Stendal, H., Mapeo, R.B.M., 2009. Characterization of enriched lithospheric mantle components in ~2.7 Ga banded iron formations: an example from the Tati greenstone belt, northeastern Botswana. Precambrian Res. 172, 334–356. https://doi.org/10.1016/j.precamres.2009.06.004.

Dreher, A.M., Xavier, R.P., Martini, S.L., 2005. Fragmental rocks if the igarape Bahia Cu-Au deposits, carajas minaral province, Brazil. Rev. Bras. Geociencias 35, 359–368.

Dreher, A.M., Xavier, R.P., Taylor, B.E., Martini, S.L., 2008. New geologic, fluid inclusion and stable isotope studies on the controversial Igarapé Bahia Cu-Au deposit, Carajás Province, Brazil. Miner. Deposits 43, 161–184. https://doi.org/10.1007/s00126-007-0150-6.

Feio, G.R.L., Dall'Agnol, R., Dantas, E.L., Macambira, M.J.B., Gomes, A.C.B., Sardinha, A. S., Oliveira, D.C., Santos, R.D., Santos, P.A., 2012. Geochemistry, geochronology, and origin of the Neoarchean Planalto Granite suite, Carajás, Amazonian craton: a-type or hydrated charnockitic granites? Lithos 151, 57–73. https://doi.org/10.1016/j.lithos.2012.02.020.

Feio, G.R.L., Dall'Agnol, R., Dantas, E.L., Macambira, M.J.B., Santos, J.O.S., Althoff, F.J., Soares, J.E.B., 2013. Archean granitoid magmatism in the Canaã dos Carajás area: implications for crustal evolution of the Carajás province, Amazonian craton, Brazil. Precambrian Res. 227, 157–185. https://doi.org/10.1016/j.precamres.2012.04.007.

Galarza, M.A., Macambira, M.J.B., Villas, R.N., 2008. Dating and isotopic characteristics (Pb and S) of the Fe oxide-Cu-Au-U-REE Igarapé Bahia ore deposit, Carajás mineral province, Pará state, Brazil. J. South Am. Earth Sci. 25, 377–397. https://doi.org/10.1016/j.jsames.2007.07.006.

Gibbs, A.K., Wirth, K.R., Hirata, W.K., Olszewski Jr., W.J., 1986. Age and composition of the grão pará groups volcanics, serra dos Carajás. Rev. Bras. Geociencias 16, 201–211.

Hagadorn, J.W., Bottjer, D.J., 1997. Wrinkle structures: microbially mediated sedimentary structures common in subtidal siliciclastic settings at the Proterozoic-Phanerozoic transition. Geology 25, 1047–1050. https://doi.org/10.1130/0091-7613(1997)025<1047:WSMMSS>2.3.CO;2.

Hagemann, S.G., Angerer, T., Duuring, P., Rosière, C.A., Figueiredo e Silva, R.C., Lobato, L., Hensler, A.S., Walde, D.H.G., 2016. BIF-hosted iron mineral system: a review. Ore Geol. Rev. 76, 317–359. https://doi.org/10.1016/j.oregeorev.2015.11.004.

Heimann, A., Johnson, C.M., Beard, B.L., Valley, J.W., Roden, E.E., Spicuzza, M.J., Beukes, N.J., 2010. Fe, C, and O isotope compositions of banded iron formation carbonates demonstrate a major role for dissimilatory iron reduction in ~2.5Ga marine environments. Earth Planet Sci. Lett. 294, 8–18. https://doi.org/10.1016/j.epsl.2010.02.015.

Isley, A.E., 1995. Hydrothermal plumes and the delivery of iron to banded iron formation. J. Geol. 103, 169–185. https://doi.org/10.1086/629734.

Isley, A.E., Abbott, D.H., 1999. Plume-related mafic volcanism and the deposition of banded iron formation. J. Geophys. Res. Solid Earth 104, 15461–15477. https://doi.org/10.1029/1999jb900066.

Jackson, G.D., Hunt, P.A., Loveridge, W.D., Parrish, R.R., 1990. Reconnaissance geochronology of baffin island, N.W.T. Radiogenic age isot. Stud. Rep. 3 Geol. Surv. Canada Pap. 89-2 (3), 123–148.

Johnson, C.M., Ludois, J.M., Beard, B.L., Beukes, N.J., Heimann, A., 2013. Iron formation carbonates: paleoceanographic proxy or recorder of microbial diagenesis? Geology 41, 1147–1150. https://doi.org/10.1130/G34698.1.

Justo, A.P., Dantas, E.L., Bau, M., Freitas-Silva, F.H., Santos, R.V., Schorscher, J.H.D., 2020. Paleobasinal to band-scale REE+Y distribution in iron formations from Carajás amazon craton, Brazil. Ore Geol. Rev. 103750 https://doi.org/10.1016/j.oregeorev.2020.103750.

Klein, C., 2005. Some Precambrian banded iron-formations (BIFs) from around the world: their age, geologic setting, mineralogy, metamorphism, geochemistry, and origin. Am. Mineral. 90, 1473–1499. https://doi.org/10.2138/am.2005.1871.

Klein, C., Ladeira, E.A., 2002. Petrography and geochemistry of the least altered banded iron-formation of the archean carajas formation, northern Brazil. Econ. Geol. 97, 643–651. https://doi.org/10.2113/97.3.643.

Konhauser, K.O., Planavsky, N.J., Hardisty, D.S., Robbins, L.J., Warchola, T.J., Haugaard, R., Lalonde, S.V., Partin, C.A., Oonk, P.B.H., Tsikos, H., Lyons, T.W., Bekker, A., Johnson, C.M., 2017. Iron formations: a global record of Neoarchaean to Palaeoproterozoic environmental history. Earth Sci. Rev. 172, 140–177. https://doi.org/10.1016/j.earscirev.2017.06.012.

Konhauser, K.O., Robbins, L.J., Alessi, D.S., Flynn, S.L., Gingras, M.K., Martinez, R.E., Kappler, A., Swanner, E.D., Li, Y.L., Crowe, S.A., Planavsky, N.J., Reinhard, C.T., Lalonde, S.V., 2018. Phytoplankton contributions to the trace-element composition of Precambrian banded iron formations. Bull. Geol. Soc. Am. 130, 941–951. https://doi.org/10.1130/B31648.1.

Krymsky, R.S., Macambira, M.J.B., Lafon, J.-M., Estumano, G.S., 2007. Uranium-lead dating method at the Pará-Iso isotope geology laboratory, UFPA, Belém - Brazil. An. Acad. Bras. Cienc. 79, 115–128. https://doi.org/10.1590/S0001-37652007000100014.

Kump, L.R., Barley, M.E., 2007. Increased subaerial volcanism and the rise of atmospheric oxygen 2.5 billion years ago. Nature 448, 1033–1036. https://doi.org/10.1038/nature06058.

Kwelwa, S.D., Sanislav, I.V., Dirks, P.H.G.M., Blenkinsop, T., Kolling, S.L., 2018. Zircon U-Pb ages and Hf isotope data from the Kukuluma Terrain of the Geita Greenstone Belt, Tanzania Craton: implications for stratigraphy, crustal growth and timing of gold mineralization. J. Afr. Earth Sci. 139, 38–54. https://doi.org/10.1016/j.jafrearsci.2017.11.027.

Lacasse, C.M., Ganade, C.E., Mathieu, L., Teixeira, N.A., Lopes, L.B.L., Monteiro, C.F., 2020. Restoring original composition of hydrothermally altered Archean metavolcanic rocks of the Carajás Mineral Province (Brazil): geodynamic implications for the transition from lid to mobile tectonics. Lithos 372–373. https://doi.org/10.1016/j.lithos.2020.105647, 105647.

Lantink, M.L., 2022. Milankovitch cycles in banded iron formations constrain the Earth-Moon system 2.46 billion years ago. Proc. Natl. Acad. Sci. USA 119, e2117146119. https://doi.org/10.1073/pnas.2117146119/-/DCSupplemental.Published.

Lantink, M.L., Davies, J.H.F.L., Mason, P.R.D., Schaltegger, U., Hilgen, F.J., 2019. Climate control on banded iron formations linked to orbital eccentricity. Nat. Geosci. 12, 369–374. https://doi.org/10.1038/s41561-019-0332-8.

Lawrence, R.L., Cox, R., Mapes, R.W., Coleman, D.S., 2011. Hydrodynamic fractionation of zircon age populations. Geol. Soc. Am. Bull. 123, 295–305. https://doi.org/10.1130/B30151.1.

Liebmann, J., Spencer, C.J., Kirkland, C.L., Ernst, R.E., 2022. Large igneous provinces track fluctuations in subaerial exposure of continents across the Archean–Proterozoic transition. Terra. Nova 323–329. https://doi.org/10.1111/ter.12594.

Lindenmayer, Z.G., Laux, J.H., Teixeira, J.B.G., 2001. Considerações sobre a origem das formações ferríferas da Formação Carajás, Serra dos Carajás. Rev. Bras. Geociencias 31, 21–28. https://doi.org/10.25249/0375-7536.20013112128.

Lowe, D.R., LoPiccolo, R.D., 1974. The characteristics and origins of dish and pillar structures. J. Sediment. Res. 44, 484–501. https://doi.org/10.1306/74d72a68-2b21-11d7-8648000102c1865d.

Ludwig, K.R., 2012. User's manual for a geochronological toolkit for microsoft excel. Berkeley Geochronological Cent 75.

Ludwig, K.R., 1998. On the treatment of concordant uranium-lead ages. Geochem. Cosmochim. Acta 62, 665–676. https://doi.org/10.1016/S0016-7037(98)00059-3.

Macambira, M.J.B., Schrank, A., 2002. Químio-estratigrafia e evolução dos jaspilitos da Formação Carajás (PA). Rev. Bras. Geociencias 32, 567–578. https://doi.org/10.25249/0375-7536.2002324567578.

Macambira, M.J.B., Vasquez, M.L., Silva, D.C.C., Galarza, M.A., Barros, C.E.M., Camelo, J.F., 2009. Crustal growth of the central-eastern Paleoproterozoic domain, SW Amazonian craton: juvenile accretion vs. reworking. J. South Am. Earth Sci. 27, 235–246. https://doi.org/10.1016/j.jsames.2009.02.001.

Machado, N., Lindenmayer, Z., Krogh, T.E., Lindenmayer, D., 1991. U-Pb geochronology of Archean magmatism and basement reactivation in the Carajás area, Amazon shield, Brazil. Precambrian Res. 49, 329–354. https://doi.org/10.1016/0301-9268(91)90040-H.

Mansur, E.T., Ferreira Filho, C.F., 2016. Magmatic structure and geochemistry of the luanga mafic–ultramafic complex: further constraints for the PGE-mineralized magmatism in Carajás, Brazil. Lithos 266–267, 28–43. https://doi.org/10.1016/j.lithos.2016.09.036.

Marangoanha, B., de Oliveira, D.C., Galarza, M.A., Marques, G.T., 2020. Crustal anatexis and mantle-derived magmas forming Neoarchean A-type granitoids in Carajás Province, northern Brazil: petrological evidence and tectonic control. Precambrian Res. 338, 105585 https://doi.org/10.1016/j.precamres.2019.105585.

Marangoanha, B., Oliveira, D.C., Dall'Agnol, R., 2019a. The Archean granulite-enderbite complex of the northern Carajás province, Amazonian craton (Brazil): origin and implications for crustal growth and cratonization. Lithos 350–351. https://doi.org/10.1016/j.lithos.2019.105275, 105275.

Marangoanha, B., Oliveira, D.C., Oliveira, V.E.S., Galarza, M.A., Lamarão, C.N., 2019b. Neoarchean A-type granitoids from Carajás province (Brazil): new insights from geochemistry, geochronology and microstructural analysis. Precambrian Res. 324, 86–108. https://doi.org/10.1016/j.precamres.2019.01.010.

Martins, P.L.G., Toledo, C.L.B., Silva, A.M., Chemale, F., Archer, C., de Assis, L.M., 2021. Chemostratigraphy of the Carajás banded iron formation, Brazil: a record of Neoarchean Ocean chemistry. Gondwana Res. https://doi.org/10.1016/j.gr.2021.09.008.

Martins, P.L.G., Toledo, C.L.B., Silva, A.M., Chemale, F., Santos, J.O.S., Assis, L.M., 2017. Neoarchean magmatism in the southeastern Amazonian Craton, Brazil: petrography, geochemistry and tectonic significance of basalts from the Carajás Basin. Precambrian Res. 302, 340–357. https://doi.org/10.1016/j.precamres.2017.10.013.

Martinsen, O., 1994. Mass movements. In: Maltman, A. (Ed.), The Geological Deformation of Sediments. Springer Science, pp. 129–165. https://doi.org/10.1007/978-94-011-0731-0.

Melo, G.H.C., Monteiro, L.V.S., Xavier, R.P., Moreto, C.P.N., Arquaz, R.M., Silva, M.A.D., 2019. Evolution of the Igarapé Bahia Cu-Au deposit, Carajás province (Brazil): early syngenetic chalcopyrite overprinted by IOCG mineralization. Ore Geol. Rev. 111, 102993 https://doi.org/10.1016/j.oregeorev.2019.102993.

Melo, G.H.C., Monteiro, L.V.S., Xavier, R.P., Moreto, C.P.N., Santiago, E.S.B., Dufrane, S.A., Aires, B., Santos, A.F.F., 2017. Temporal evolution of the giant Salobo IOCG deposit, Carajás Province (Brazil): constraints from paragenesis of hydrothermal alteration and U-Pb geochronology. Miner. Deposits 52, 709–732. https://doi.org/10.1007/s00126-016-0693-5.

Merle, R., Caroff, M., Girardeau, J., Cotten, J., Guivel, C., 2005. Segregation vesicles, cylinders, and sheets in vapor-differentiated pillow lavas: examples from Tore-Madeira Rise and Chile Triple Junction. J. Volcanol. Geoth. Res. 141, 109–122. https://doi.org/10.1016/j.jvolgeores.2004.09.007.

Moreto, C.P.N., Monteiro, L.V.S., Xavier, R.P., Creaser, R.A., Dufrane, S.A., Melo, G.H.C., Delinardo da Silva, M.A., Tassinari, C.C.G., Sato, K., 2015a. Timing of multiple hydrothermal events in the iron oxide–copper–gold deposits of the Southern Copper Belt, Carajás Province, Brazil. Miner. Depos. 50, 517–546. https://doi.org/10.1007/s00126-014-0549-9.

Moreto, C.P.N., Monteiro, L.V.S., Xavier, R.P., Creaser, R.A., DuFrane, S.A., Tassinari, C.C.G., Sato, K., Kemp, A.I.S., Amaral, W.S., 2015b. Neoarchean and paleoproterozoic iron oxide-copper-gold events at the sossego deposit, Carajás Province, Brazil: Re-Os and U-Pb geochronological evidence. Econ. Geol. 110, 809–835. https://doi.org/10.2113/econgeo.110.3.809.

Mulder, T., Alexander, J., 2001. The physical character of subaqueous sedimentary density flows and their deposits. Sedimentology 48, 269–299. https://doi.org/10.1046/j.1365-3091.2001.00360.x.

Myrow, P.M., Tice, L., Archuleta, B., Clark, B., Taylor, J.F., Ripperdan, R.L., 2004. Flat-pebble conglomerate: its multiple origins and relationship to metre-scale depositional cycles. Sedimentology 51, 973–996. https://doi.org/10.1111/j.1365-3091.2004.00657.x.

Noffke, N., Gerdes, G., Klenke, T., Krumbein, W.E., 2001. Microbially induced sedimentary structures - a new category within the classification of primary sedimentary structures. J. Sediment. Res. 71, 649–656. https://doi.org/10.1306/d4268d60-2b26-11d7-8648000102c1865d.

Olszewski, W.J., Wirth, K.R., Gibbs, A.K., Gaudette, H.E., 1989. The age, origin, and tectonics of the Grão Pará Group and associated rocks, Serra dos Carajás, Brazil: archean continental volcanism and rifting. Precambrian Res. 42, 229–254. https://doi.org/10.1016/0301-9268(89)90013-2.

Perelló, J., Zulliger, G., García, A., Creaser, R.A., 2023. Revisiting the IOCG geology and age of alemão in the Igarapé Bahia camp, Carajás province, Brazil. J. South Am. Earth Sci. 124, 104273 https://doi.org/10.1016/j.jsames.2023.104273.

Pidgeon, R.T., MacAmbira, M.J.B., Lafon, J.M., 2000. Th-U-Pb isotopic systems and internal structures of complex zircons from an enderbite from the Pium Complex, Carajas Province, Brazil: evidence for the ages of granulite facies metamorphism and the protolith of the enderbite. Chem. Geol. 166, 159–171. https://doi.org/10.1016/S0009-2541(99)00190-4.

Pinheiro, R.V.L., Holdsworth, R.E., 1997. Reactivation of Archaean strike-slip fault systems, Amazon region, Brazil. J. Geol. Soc. London. 154, 99–103. https://doi.org/10.1144/gsjgs.154.1.0099.

Postma, G., 1990. Depositional architecture and facies of river and fan deltas: a synthesis. In: Collela, A., David, B.P. (Eds.), Coarse-Grained Deltas. International Association of Sedimentology Special Publication, pp. 13–28.

Rasmussen, B., Meier, D.B., Krapež, B., Muhling, J.R., 2013. Iron silicate microgranules as precursor sediments to 2.5-billion-year-old banded iron formations. Geology 41, 435–438. https://doi.org/10.1130/G33828.1.

Ravier, E., Guiraud, M., Guillien, A., Vennin, E., Buoncristiani, J.-F., Portier, E., 2015. Micro- to macro-scale internal structures, diagenesis and petrophysical evolution of injectite networks in the Vocontian Basin (France): implications for fluid flow. Mar. Petrol. Geol. 64, 125–151. https://doi.org/10.1016/j.marpetgeo.2015.02.040.

Rego, E.S., Busigny, V., Lalonde, S.V., Philippot, P., Bouyon, A., Rossignol, C., Babinski, M., Zapparoli, A., 2021. Anoxygenic photosynthesis linked to Neoarchean iron formations in Carajás (Brazil). Geobiology 19, 326–341. https://doi.org/10.1111/gbi.12438.

Rego, E.S., Busigny, V., Lalonde, S.V., Rossignol, C., Babinski, M., Philippot, P., 2023. Low-phosphorus concentrations and important ferric hydroxide scavenging in Archean seawater. PNAS Nexus 2, 1–7. https://doi.org/10.1093/pnasnexus/pgad025.

Requia, K., Stein, H., Fontboté, L., Chiaradia, M., 2003. Re-Os and Pb-Pb geochronology of the Archean Salobo iron oxide copper-gold deposit, Carajás mineral province, northern Brazil. Miner. Deposits 38, 727–738. https://doi.org/10.1007/s00126-003-0364-1.

Ribeiro da Luz, B., Crowley, J.K., 2012. Morphological and chemical evidence of stromatolitic deposits in the 2.75Ga Carajás banded iron formation, Brazil. Earth Planet Sci. Lett. 355–356, 60–72. https://doi.org/10.1016/j.epsl.2012.08.028.

Ronze, P.C., Soares, A.D.V., Santos, M.G.S., Barreira, C.F., 2000. Alemao copper-gold (U-REE) deposits, Carajas, Brazil. In: Porter, T.M. (Ed.), Hydrothermal Iron Oxide Copper-Gold and Related Deposits: A Global Perspective. PCG Publishing, pp. 191–202.

Rossignol, C., Antonio, P.Y.J., Narduzzi, F., Rego, E.S., Teixeira, L., de Souza, R.A., Ávila, J.N., Silva, M.A.L., Lana, C., Trindade, R.I.F., Philippot, P., 2022. Unraveling one billion years of geological evolution of the southeastern Amazonia Craton from detrital zircon analyses. Geosci. Front. 13, 101202 https://doi.org/10.1016/j.gsf.2021.101202.

Rossignol, C., Bourquin, S., Poujol, M., Hallot, E., Dabard, M.-P., Nalpas, T., 2016. The volcaniclastic series from the Luang Prabang Basin, Laos: a witness of a triassic magmatic arc? J. Asian Earth Sci. 120 https://doi.org/10.1016/j.jseaes.2016.02.001.

Rossignol, C., Hallot, E., Bourquin, S., Poujol, M., Jolivet, M., Pellenard, P., Ducassou, C., Nalpas, T., Heilbronn, G., Yu, J., Dabard, M.-P., 2019. Using volcaniclastic rocks to constrain sedimentation ages: To what extent are volcanism and sedimentation synchronous? Sediment. Geol. 381, 46–64. https://doi.org/10.1016/J.SEDGEO.2018.12.010.

Rossignol, C., Rego, E.S., Narduzzi, F., Teixeira, L., Ávila, J.N., Silva, M.A.L., Lana, C., Philippot, P., 2020. Stratigraphy and geochronological constraints of the serra sul formation (Carajás Basin, amazonian craton, Brazil). Precambrian Res. 351, 105981 https://doi.org/10.1016/j.precamres.2020.105981.

Rubatto, D., 2002. Zircon trace element geochemistry: partitioning with garnet and the link between U–Pb ages and metamorphism. Chem. Geol. 184, 123–138. https://doi.org/10.1016/S0009-2541(01)00355-2.

Sardinha, A.S., Barros, C.E.M., Krymsky, R., 2006. Geology, geochemistry, and U-Pb geochronology of the archean (2.74 Ga) serra do rabo granite stocks, Carajás metallogenetic province, northern Brazil. J. South Am. Earth Sci. 20, 327–339. https://doi.org/10.1016/j.jsames.2005.11.001.

Siepierski, L., Ferreira Filho, C.F., 2020. Magmatic structure and petrology of the Vermelho Complex, Carajás Mineral Province, Brazil: evidence for magmatic processes at the lower portion of a mafic-ultramafic intrusion. J. South Am. Earth Sci. 102, 102700 https://doi.org/10.1016/j.jsames.2020.102700.

Siepierski, L., Ferreira Filho, C.F., 2016. Spinifex-textured komatiites in the south border of the carajas ridge, selva greenstone belt, Carajás province, Brazil. J. South Am. Earth Sci. 66, 41–55. https://doi.org/10.1016/j.jsames.2015.12.011.

Silva, F.F., Oliveira, D.C., Dall'Agnol, R., Silva, L.R., Cunha, I.V., 2020. Lithological and structural controls on the emplacement of a Neoarchean plutonic complex in the Carajás province, southeastern Amazonian craton (Brazil). J. South Am. Earth Sci. 102, 102696 https://doi.org/10.1016/j.jsames.2020.102696.

Simonson, B.M., Goode, A.D.T., 1989. First discovery of ferruginous chertarenites in the early Precambrian Hamersley Group of western Australia. Geology 17, 269–272.

Simonson, B.M., Hassler, S.W., 1996. Was the deposition of large precambrian iron formations linked to major marine transgressions? J. Geol. 104, 665–676. https://doi.org/10.1086/629861.

Slabunov, A.I., Nesterova, N.S., Egorov, A.V., Kuleshevich, L.V., Kevlich, V.I., 2021. Age of the archean strata with banded Iron Formation in the kostomuksha greenstone belt, Karelian craton, fennoscandian shield: constraints on the geochemistry and geochronology of zircons. Geochem. Int. 59, 341–356. https://doi.org/10.1134/S0016702921040066.

Smith, A.J.B., Beukes, N.J., Gutzmer, J., 2013. The composition and depositional environments of mesoarchean iron formations of the west rand group of the witwatersrand Supergroup, South Africa. Econ. Geol. 108, 111–134. https://doi.org/10.2113/econgeo.108.1.111.

Sohn, Y.K., Park, K.H., Yoon, S.-H., 2008. Primary versus secondary and subaerial versus submarine hydrovolcanic deposits in the subsurface of Jeju Island, Korea. Sedimentology 55, 899–924. https://doi.org/10.1111/j.1365-3091.2007.00927.x.

Souza, S.R.C., Botelho, N.F., Dantas, E.L., Jiménez, F.A.C., Reis, M.A., Viana, C.S., 2020. Geochemistry and isotopic geology of the lagoa seca gold deposit in the andorinhas greenstone-belt, Carajás province, Brazil. J. South Am. Earth Sci. 99, 102523 https://doi.org/10.1016/j.jsames.2020.102523.

Spier, C.A., de Oliveira, S.M.B., Sial, A.N., Rios, F.J., 2007. Geochemistry and genesis of the banded iron formations of the cauê formation, quadrilátero ferrífero, Minas Gerais, Brazil. Precambrian Res. 152, 170–206. https://doi.org/10.1016/j.precamres.2006.10.003.

Sunder Raju, P.V., Mazumder, R., 2020. Archean sedimentation on dharwar craton, India and its implications. Earth Sci. Rev. https://doi.org/10.1016/j.earscirev.2019.102999.

Tallarico, F.H.B., Figueiredo, B.R., Groves, D.I., Kositcin, N., McNaughton, N.J., Fletcher, I.R., Rego, J.L., 2005. Geology and SHRIMP U-Pb geochronology of the Igarapé Bahia deposit, Carajás copper-gold belt, Brazil: an Archean (2.57 Ga) example of Iron-Oxide Cu-Au-(U-REE) mineralization. Econ. Geol. 100, 7–28. https://doi.org/10.2113/100.1.0007.

Tavares, F.M., Trouw, R.A.J., da Silva, C.M.G., Justo, A.P., Oliveira, J.K.M., 2018. The multistage tectonic evolution of the northeastern Carajás Province, Amazonian Craton, Brazil: revealing complex structural patterns. J. South Am. Earth Sci. 88, 238–252. https://doi.org/10.1016/j.jsames.2018.08.024.

Tolbert, G.E., Tremaine, J.W., Melcher, G.C., Gomes, C.B., 1971. The recently discovered serra dos Carajás iron deposits, northern Brazil. Econ. Geol. 66, 985–994. https://doi.org/10.2113/gsecongeo.66.7.985.

Toledo, P.I.F., Moreto, C.P.N., Xavier, R.P., Gao, J.F., de Matos, J.H.S.N., de Melo, G.H.C., 2019. Multistage evolution of the Neoarchean (ca. 2.7 Ga) Igarapé cinzento (GT-46) iron oxide copper-gold deposit, Cinzento shear zone, Carajás Province, Brazil. Econ. Geol. 114, 1–34. https://doi.org/10.5382/econgeo.2019.4617.

Trendall, A.F., 2002. The significance of iron-formation in the Precambrian stratigraphic record. In: Altermann, W., Corcoran, P.L. (Eds.), Special Publication of the International Association of Sedimentologists. International Association of Sedimentologists Special Publication, pp. 33–66.

Trendall, A.F., Basei, M.A.S., De Laeter, J.R., Nelson, D.R., 1998. SHRIMP zircon U-Pb constraints on the age of the carajas formation, grao para group, amazon craton. J. South Am. Earth Sci. 11, 265–277. https://doi.org/10.1016/S0895-9811(98)00015-7.

Vasquez, M.L., Sousa, C.S., Carvalho, J.M.A., 2008. Mapa Geológico Do Estado Do Pará. Scale 11 000 000.

Viehmann, S., Bau, M., Hoffmann, J.E., Münker, C., 2015. Geochemistry of the Krivoy Rog Banded Iron Formation, Ukraine, and the impact of peak episodes of increased global magmatic activity on the trace element composition of Precambrian seawater. Precambrian Res. 270, 165–180. https://doi.org/10.1016/j.precamres.2015.09.015.

Wignall, P., 2005. The link between large igneous province eruptions and mass extinctions. Elements 1, 293–297. https://doi.org/10.2113/gselements.1.5.293.

Wirth, K.R., Gibbs, A.K., Olszewski, W.J., 1986. U-Pb ages of zircons from the grão-pará group and serra dos Carajás granites, pará, Brazil. Rev. Bras. Geociencias 16, 195–200.